International Journal of Chemical Engineering

Thermal Catalytic Synthesis of Biofuels and High-Value Chemicals

Lead Guest Editor: Heng Zhang
Guest Editors: Hu Li and Putla Sudarsanam

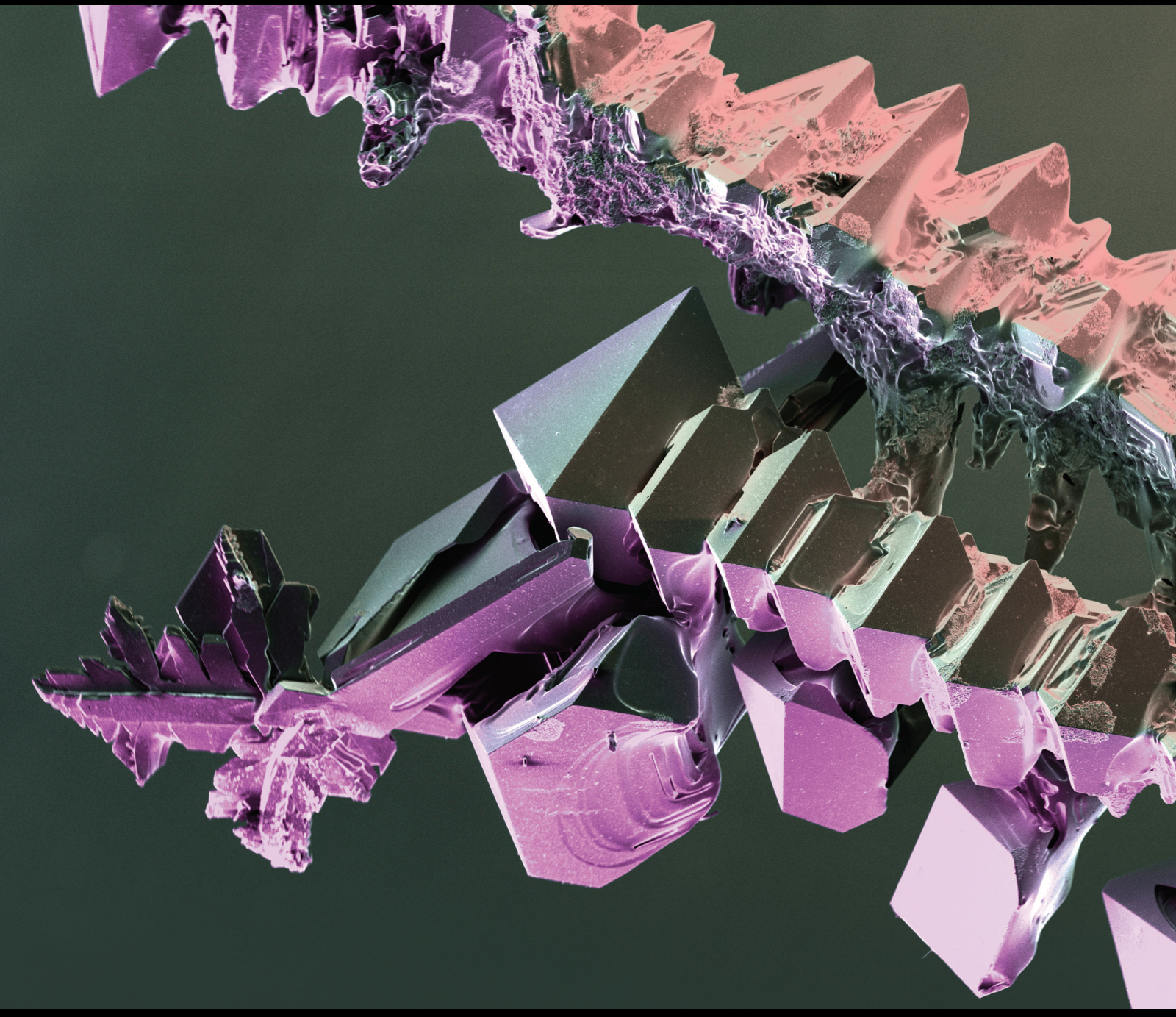

Thermal Catalytic Synthesis of Biofuels and High-Value Chemicals

International Journal of Chemical Engineering

Thermal Catalytic Synthesis of Biofuels and High-Value Chemicals

Lead Guest Editor: Heng Zhang
Guest Editors: Hu Li and Putla Sudarsanam

Contents

Hindawi
International Journal of Chemical Engineering
Volume 2021, Article ID 8971613, 11 pages
https://doi.org/10.1155/2021/8971613

Review Article

Efficient Synthesis of Biodiesel Catalyzed by Chitosan-Based Catalysts

Anping Wang,[1] **Wenxuan Quan**,[1] **and Heng Zhang**[2]

[1]*Key Laboratory for Information System of Mountainous Area and Protection of Ecological Environment of Guizhou Province, Guizhou Normal University, Guiyang, Guizhou 550025, China*
[2]*State Key Laboratory Breeding Base of Green Pesticide & Agricultural Bioengineering, Key Laboratory of Green Pesticide & Agricultural Bioengineering, Ministry of Education, State-Local Joint Laboratory for Comprehensive Utilization of Biomass, Center for Research & Development of Fine Chemicals, Guizhou University, Guiyang, Guizhou 550025, China*

Correspondence should be addressed to Wenxuan Quan; wenxuanq@gznu.edu.cn and Heng Zhang; hzhang23@gzu.edu.cn

Received 9 July 2021; Revised 16 November 2021; Accepted 17 November 2021; Published 29 December 2021

Academic Editor: Prem Kumar Seelam

Catalysts play an important role in the preparation of biodiesel. It is of great significance to study catalysts with high efficiency, low cost, and easy preparation. Compared with the homogeneous catalyst system, the heterogeneous catalyst is easy to separate and has a better catalytic effect. In heterogeneous catalysts, supports and preparation methods have important effects on the dispersion of active centers and the overall performance of catalysts. However, the supports of existing solid catalysts have defects in porosity, structural uniformity, stability, and specific surface area, and the preparation methods cannot stabilize covalent bonds or ionic bonds to bind catalytic sites. Considering the activity, preparation method, and cost of the catalyst, biomass-based catalyst is the best choice, but the specific surface area of the biomass-based catalyst is relatively low, the distribution of active centers is uneven, and it is easy to lose. Therefore, the hybrid carrier of biomass-based catalyst and other materials can not only improve the specific surface area but also make the distribution of active centers uniform and the catalytic activity better. Based on this, we summarized the application of chitosan hybrid material catalysts in biodiesel. The preparation, advantages and disadvantages, reaction conditions, and so on of chitosan-based catalysts were mainly concerned. At the same time, exploring the effects of different types of chitosan-based catalysts on the preparation of biodiesel and exploring the process technology with high efficiency and low consumption is the focus of this paper.

1. Introduction

In recent decades, with the accelerated development of industrialization, global fossil fuel consumption and greenhouse gas emissions have increased rapidly. Scientists predict that the total global energy consumption will increase by 28% from 2015 to 2040 [1]. However, traditional energy, which is the main source of global energy supply, is constantly consumed, leading to energy shortage. This problem has attracted the attention of researchers all over the world, who are looking for sustainable and ecofriendly alternative energy [2, 3]. Therefore, scientists try to replace fossil fuels by developing renewable green energy, among which biofuels are the most competitive. Biodiesel is the most representative liquid biofuel among biofuels. It has the advantages of green, renewable, nontoxic, and environmental protection [4]. Meanwhile, biodiesel is almost free of sulfur and aromatic substances, biodegradable, and belongs to truly renewable "green energy" [5].

First of all, the main raw materials used to prepare biodiesel are rapeseed oil, soybean oil, and other edible oils, but this has an impact on national food safety and there is a problem of competing with people for food. Later, further research showed that nonedible oils are also used as the raw materials for biodiesel production, such as *Jatropha curcas*, *Euphorbia lathyris* [6], *Xanthium sibiricum* [7], *Firmiana platanifolia* [8], and *Koelreuteria integrifoliola* [9]. This expands the raw material source of biodiesel and greatly

reduces the cost. After that, to further reduce the cost, biodiesel was prepared from waste cooking oil and animal fat with high acid value [10]. In addition, microalgae are also used as biodiesel raw materials, which is effective to reduce the cost of biodiesel, but the cultivation of microalgae also requires additional costs. In short, the new raw materials of biodiesel are of great significance for alleviating the energy crisis, protecting the ecological environment and adjusting the agricultural structure [11–13].

Biodiesel is generally a mixture of fatty acid methyl ester or ethyl ester, mainly because the raw materials for its synthesis contain many types of triglycerides [5]. The conventional method of synthesizing biodiesel are esterification and transesterification. Generally, acids [14], bases [15], and enzymes [16] are used as catalysts for biodiesel synthesis. Heterogeneous catalysts have gradually replaced homogeneous catalysts, which is mainly because heterogeneous catalysts can be reused many times, which can effectively reduce the cost [11]. Nowadays, different kinds of heterogeneous catalysts have been used to prepare biodiesel, including carbon materials [17], SiO_2 materials [18], oxides [19], ion exchange resins [20], magnetic materials [21], and supported enzymes [22]. However, the traditional solid catalyst has the disadvantages of easy loss of active sites and poor reusability. Therefore, looking for a green, efficient, and stable heterogeneous catalyst to prepare biodiesel has become one of the research hotspots for the preparation of high-performance heterogeneous catalysts [1].

Nowadays, people realize that the development of renewable and biodegradable biomass-based catalysts is more conducive to green environmental protection [23]. The excellent performance of functionalized biomass-based catalysts has attracted much attention [24]. In terms of biomass, chitosan prepared from shrimp shells and crab shells is a high molecular polymer biomass-based material. Chitosan has a large number of active –OH and $-NH_2$ groups and has strong modification ability. At the same time, chitosan is a cheap polymer material, which has natural advantages as a catalyst material in industrial production. Chitin, the raw material of chitosan, is a natural polymer compound second only to cellulose in nature. It is not only rich in resources but also widely used in medicine, food, chemical industry, cosmetics, water treatment, and other fields because of its biological function, compatibility, safety, and biodegradability [25–29].

This paper focuses on the research progress of chitosan-based catalysts in biodiesel. The synthesis method, physicochemical properties, catalytic efficiency, and reaction conditions of chitosan-based catalysts were also discussed. We hope that through this paper, we can provide new ideas for the preparation of biomass-based catalysts and obtain more efficient, green, and environmentally friendly new catalysts for the industrial synthesis of biodiesel.

2. Chitosan Derivatives

Because chitosan is easy to be modified, there are many derivatives of chitosan, which makes it possible to prepare a variety of chitosan-based catalysts, with more and more applications for the production of biodiesel.

Zhao et al. [30] prepared $CoFe_2O_4$-CS-SO_3H chitosan solid magnetic sulfonic acid catalyst for the synthesis of compounds. The preparation process of the catalyst is simple, and the obtained catalyst has strong magnetism (Figure 1).

Chitosan is a kind of polysaccharide that is easy to graft. Some researchers have tried to graft sulfonic groups onto chitosan monomers and synthesized several chitosan sulfate membranes. This makes the catalyst contain the sulfonic group and amino functional group, which further improves the activity of the catalyst [31]. Gu et al. [32] prepared chitosan-doped polyvinyl alcohol films by the blending heating method. The surfaces of these membranes are usually wrinkled and have excellent separation performance. They can be used for pervaporation to separate methanol-biodiesel mixtures. Gupta and Jabrail [33] used the glutaraldehyde crosslinking method to prepare chitosan microspheres (in Figure 2). Usually, glutaraldehyde condenses with the amino group of chitosan ammonia to form a network polymer, and the formed chemical bond crosslinks and solidifies the microspheres. In this process, the loaded particles can be wrapped in the microspheres or adsorbed on the surface of the microspheres. This is conducive to the encapsulation of internal magnetic particles and the adsorption of external catalyst particles.

Liu et al. [34] introduced a simple method for preparing magnetic chitosan Fe_3O_4 nanoparticles. Immobilized lipase was prepared by a glutaraldehyde crosslinking reaction under a 0.45 T static magnetic field. The results show that there is no significant difference in the structure of nanoparticles, the morphology of nanoparticles changes from spherical to a rod, and the magnetic properties change significantly.

Li et al. [35] prepared a series of chitosan hybrids based on polyoxometalates by anion exchange of a novel crosslinked chitosan ionic polymer with $H_3PW_{12}O_{40}$. Bodmeier et al. [36] first proposed the preparation of chitosan microspheres by the ionic gel method (in Figure 3). The polyanion of sodium tripolyphosphate is used as a crosslinking agent, which is combined with the positively charged amino group after the protonation of the chitosan molecular chain. Through the electrostatic interaction, the physical crosslinking of the molecules can be reversible, intramolecular or intramolecular, so that the chitosan can be gelated into spherical particles.

Huang et al. [37] prepared N-doped carbon prepared by chitosan with a large specific surface area. Chitosan is dissolved in acetic acid and carbonized to form porous carbon. After KOH activation, its specific surface area can reach 3532 m^2/g. The carbon-based catalyst is relatively stable and has a large specific surface area.

A new type of sustainable catalytic material was prepared from biological waste (chitosan) and rare earth–rich cobalt salt (in Figure 4). Through the chelation of chitosan with Co, the carbonized catalyst has a carbon shell containing N and encapsulates Co and Co_3O_4, which can improve the performance of the catalyst and effectively reduce the loss of active components. The catalyst has been reused many times, and the efficiency has not changed significantly [38].

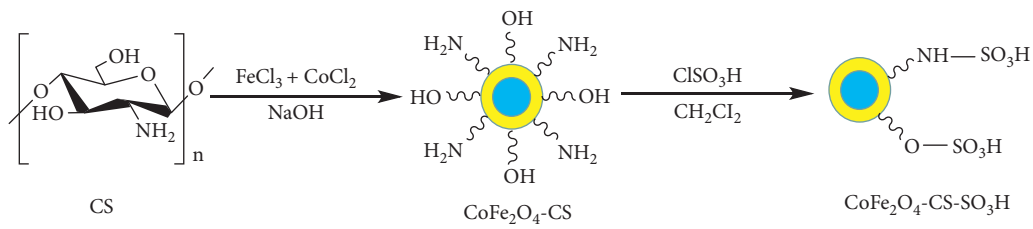

Figure 1: The preparation process of $CoFe_2O_4$-CS-SO_3H catalyst [30].

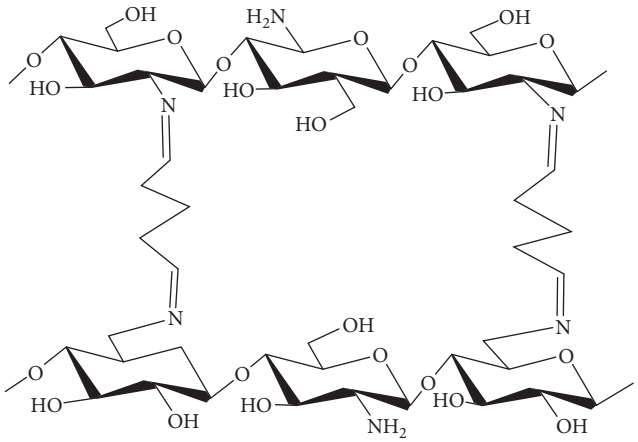

Figure 2: The microsphere formed by crosslinking chitosan and glutaraldehyde [33].

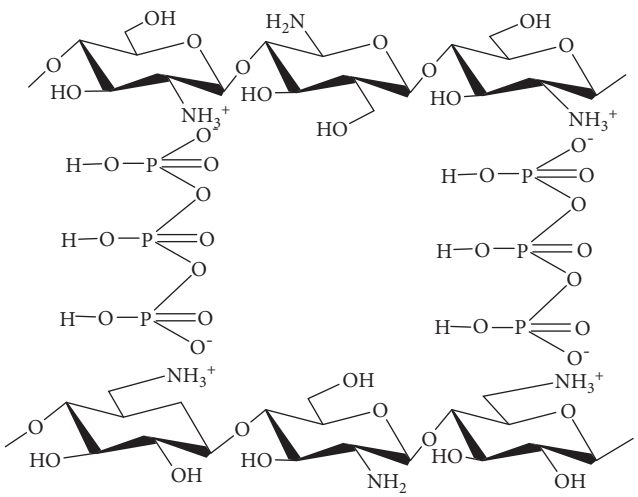

Figure 3: Structure of microspheres crosslinked by chitosan and sodium tripolyphosphate [36].

Roosen et al. [39] prepared SiO_2 chitosan composite mesoporous material with a specific surface area of 219 m^2/g, pore volume of 1.036 cm^3/g, and pore size of 9.5 nm, which belongs to mesoporous structure and is more suitable as a catalyst support material. Sana et al. [40] prepared chitosan microspheres supported a Pd catalyst, including the direct complexation of Pd^{2+} with the amino group on chitosan and the complexation of chitosan modified by glutaraldehyde with Pd^{2+}, and the complexation of chitosan modified by glutaraldehyde with Pd^{2+}. γ-Thiobutyrolactone-modified chitosan has three kinds of catalysts: sulfhydryl group and Pd^{2+}. The specific surface areas of the three catalysts are 239, 239, and 302 m^2/g, respectively. γ-Thiobutyrolactone-modified chitosan microspheres have a higher specific surface area. Also, the catalyst is used in the mixed solution of water and ethanol, so it has strong hydrophobicity. It is expected that the modified biodiesel can be used in the preparation of water-containing biodiesel.

3. Chitosan Gel and Chelating Metal Catalysts

3.1. Chitosan Gel. To reduce the production cost of biodiesel, more and more kitchen waste oil, non-edible vegetable oil, and microalgae oil are used as raw materials of biodiesel. However, these raw materials contain a large amount of free fatty acids (FFA). The key to the synthesis of biodiesel is to find heterogeneous catalysts that can simultaneously catalyze esterification and transesterification. Kayser and Pienkoß [41] evaluated the transesterification with chitosan and frozen gel as catalysts for different oils and methanol. As a green waste and a catalyst for biofuel production, chitosan can increase new possibilities for local value. Chitosan freeze-gel successfully catalyzed transesterification of three oleic glycerin and soybean oil with methanol and achieved a yield of 90% of biodiesel at 8 to 32 hours at 100–150°C. The chitosan beads were washed with tertbutyl alcohol and methanol, and the fat and glycerin were desorbed. To achieve practical use, further research and development opportunities can be identified at the catalyst design level, and new catalysts based on chitosan, such as aerogels, layers, and chitosan derivatives can be used to achieve more efficient catalytic activity and will show a greater degree of recyclable results.

3.2. Chitosan Chelating Metal Catalysts. Da Silva et al. [42] used chitosan-adsorbed Cu (II) and Co (II) catalysts for transesterification of soybean and babassu oil. The maximum adsorption capacities of copper and cobalt ions were 1.584 and 1.260 mg, respectively, while the oil conversion of biodiesel was higher when using chitosan-adsorbed Co (II) as a catalyst.

4. Acidic Modified Chitosan Catalysts

4.1. Sulfonic Acid. Based on the fact that chitosan is easy to crosslink, a new type of acidic chitosan membrane (ACM) was formed by crosslinking chitosan with sulfosuccinic acid (SSA). The esterification reaction of oleic acid and methanol was carried out to test the catalytic effect (in Figure 5). The acid

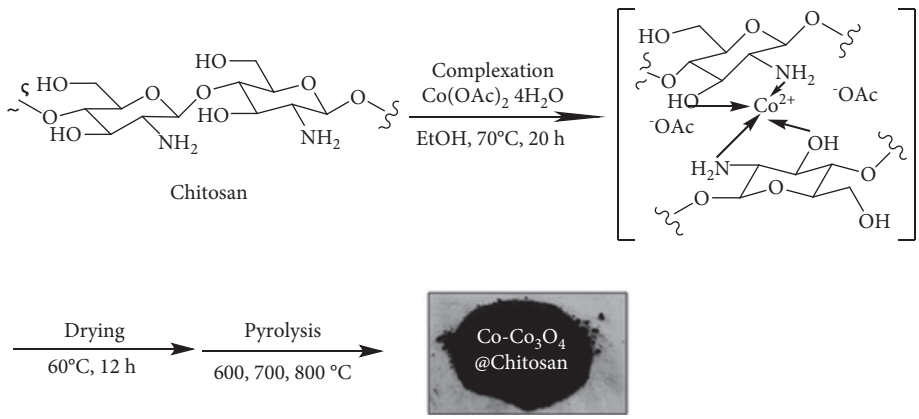

Figure 4: Synthesis of Co-Co_3O_4@chitosan materials. [38].

density of ACM was 4.62 mmol/g, which was only slightly lower than that of Amberlyst-15 (4.76 mmol/g). Under the same conditions, the catalytic efficiency of Amberlyst-15 was only 44.30%, while that of ACM was 98.76%. The reaction conditions were optimized by combining a single factor test with the response surface method. The catalytic activity of ACM for esterification of fatty acids with alcohols was studied. In addition, the reusability of ACM is also studied [43]. In conclusion, the active sites are more exposed after chitosan crosslinking, which is beneficial to the catalytic reaction, which is also the reason why ACM has higher catalytic efficiency.

Caetano et al. [44] studied the esterification of palmitic acid with methanol at 60°C. The sulfonic group was introduced into chitosan (CT) by crosslinking with sulfosuccinic acid (SSA). With the increase of sulfonic group content in chitosan, the catalytic activity increased. However, with the increase of sulfonic group content, the catalytic activity decreased. This kind of behavior can be explained by the factors of limiting diffusion. The catalytic stability of CT4 (2.08 mmol sulfonic group/g) was evaluated by using the same catalyst samples for continuous batch operation. After the second batch reaction, the catalytic activity tends to be stable. CT4 catalyst is also used for esterification of oleic acid and stearic acid with methanol. CT4 has good catalytic activity for different substrates used in esterification. It is confirmed that chitosan is a kind of biopolymer rich in the sulfonic group, and it is an efficient and environmentally friendly heterogeneous catalyst.

Wang et al. [45] prepared a chitosan sulfonic acid catalyst by a relatively simple method. The specific method is to disperse chitosan with dichloromethane as the solvent and then sulfonate chitosan with chlorosulfonic acid to obtain a biomass-based catalyst with an acid density up to 3.81 mmol/g. SEM results show that CS-SO_3H is spherical with a diameter of about 10 μm. After four times of reuse, the yield of the catalyst can still reach 85.7%, which indicates that this kind of sulfonic acid catalyst has a good application prospect.

4.2. Heteropoly Acid. Tong et al. [46] used $H_3PW_{12}O_{40}$, chitosan, and Ti^{4+} as carriers to prepare water-insoluble multifunctional active sites and $H_3PW_{12}O_{40}$/Ti/chitosan hybrid materials (in Figure 6). Due to the presence of B acid from $H_3PW_{12}O_{40}$, Lewis acid from Ti^{4+}, and base from $-NH_2$ group of chitosan, the catalyst showed high activity in the esterification reaction, all of which was due to the pore formation in chitosan by introducing Ti ions. Moreover, $H_3PW_{12}O_{40}$/Ti/chitosan can be reused at least 6 times as a heterogeneous catalyst; the activity reduction is not obvious, and only a small amount of Ti^{4+} and $H_3PW_{12}O_{40}$ are leached from the carrier chitosan.

Han et al. [47] prepared organic-inorganic hybrid catalysts by glycine (Gly) and phosphotungstic acid (TPA), namely $[Gl_yH]_xH_{3-x}PW_{12}O_{40}$ ($x = 1.0–3.0$), and studied the catalytic performance of various Gly-TPA catalysts in the esterification of palmitic acid with methanol to produce methyl palmitate. Under the optimum conditions, the yield of biodiesel can reach 93.3%.

4.3. Chitosan Magnetic Acid. Wang and his colleagues [48] synthesized a new magnetic mesoporous solid acid catalyst (FCHC-SO_3H) (in Figure 7). The catalyst was prepared from biodegradable chitosan with a double-shell hollow structure, which increased the active sites, and the synthesis process was mild and environmentally friendly. More importantly, the catalyst has good catalytic performance for the esterification of oleic acid and methanol to biodiesel, which can be reused 5 times without a significant decrease in activity and can be easily separated by an external magnetic field.

5. Basic-Modified Chitosan Catalysts

5.1. Inorganic Base. Used waste cooking oil (WCO) or frying oil is considered to be a rich source of economic raw materials for biodiesel production. Zeolite/chitosan/KOH composite was used as a solid heterogeneous catalyst for transesterification of WCO to methyl ester (biodiesel) (in Figure 8). The results show that the treatment of natural zeolite (clinoptilolite) with KOH can significantly reduce the silicon content and increase its K^+. The content is determined by the formation of hydroxy calcium carbonate. Electrolysis (EM) is used as a suitable technology for energy and resource recovery in waste treatment. In theory, EM can

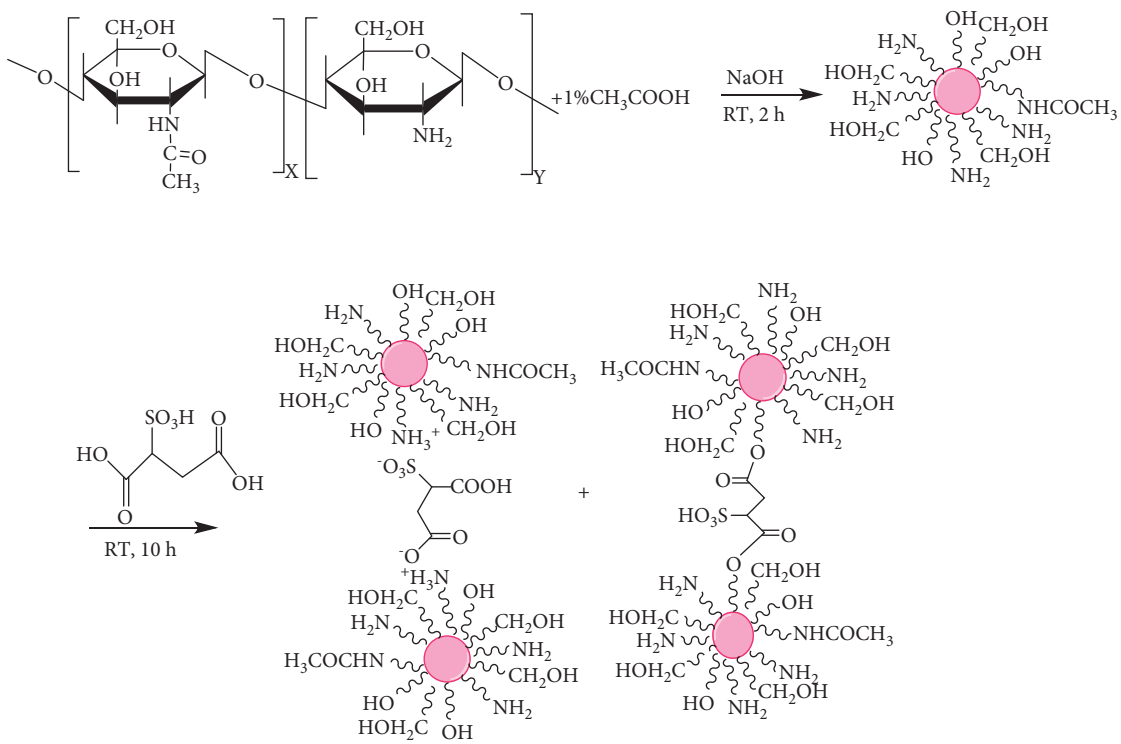

Figure 5: Synthesis of CSA catalyst. Reproduced with permission from [43] copyright 2019, Elsevier.

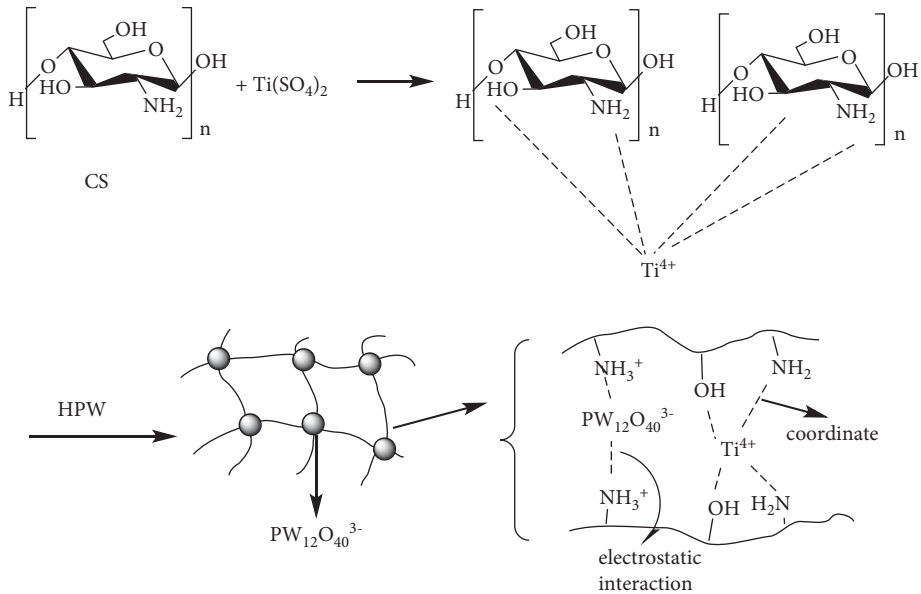

Figure 6: The preparation of HPW/Ti/chitosan hybrids. Reproduced from [46] under creative commons license (CC BY 3.0) copyright 2017, Royal Society of Chemistry.

convert any biodegradable waste into H_2, O_2, biofuel, glycerol, and other byproducts. However, the effectiveness of the system may vary greatly in different situations. In the presence of water, the conversion of biodiesel from WCO was obtained with 93% yield within 3 hours with 1% catalyst concentration and 1 : 70 alcohol/oil ratio (at 40 V) and 2% of the total solution. The best conversion process can be achieved by using acetone as the cosolvent [49].

Correia et al. [50] think that chitosan can be used as a structural agent by inserting calcium oxide and as a catalyst in transesterification. These calcium-doped chitosan spheres were calcined to obtain porous calcium catalyst without organic matter. The materials were characterized by X-ray diffraction, thermogravimetric analysis, Fourier-transform infrared spectroscopy, X-ray photoelectron spectroscopy, temperature-programmed CO_2 desorption, scanning

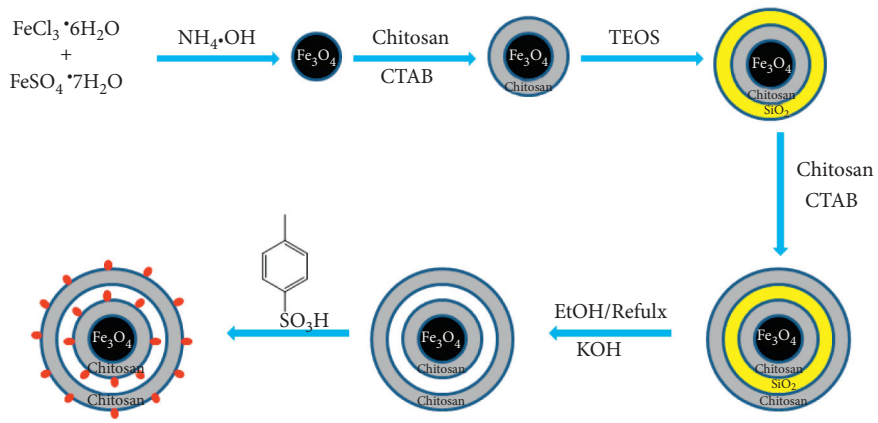

Figure 7: Synthesis of the FCHC-SO_3H catalyst. Reproduced with permission from [48] copyright 2018, Elsevier.

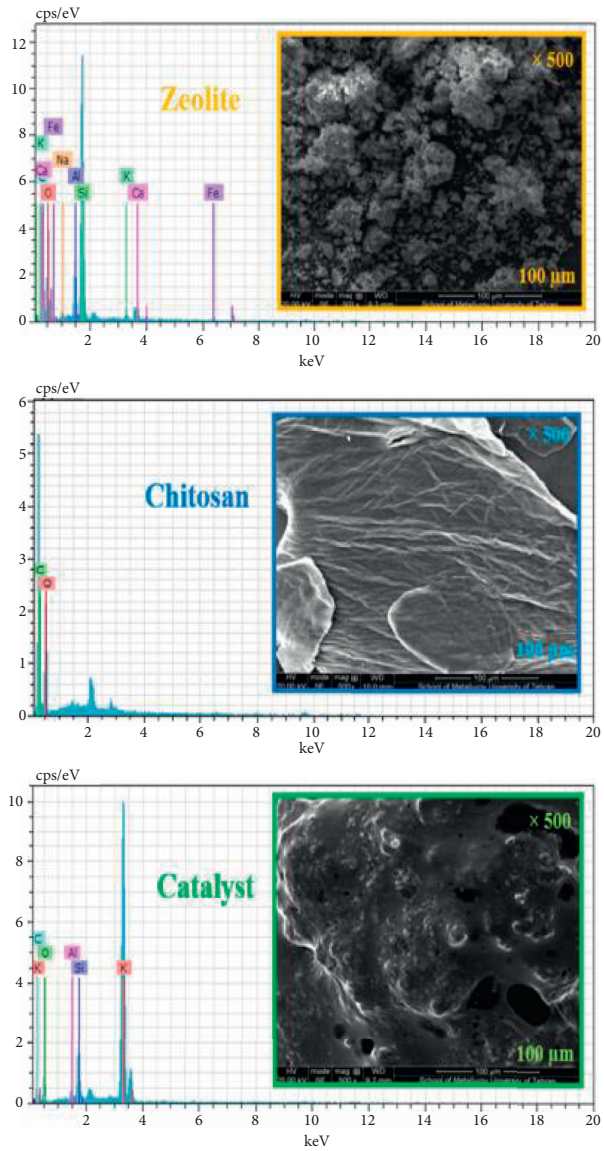

Figure 8: SEM micrographs and EDX spectra of raw zeolite, pure chitosan, and modified zeolite/chitosan/KOH catalyst. Reproduced with permission from [49] copyright 2017, Elsevier.

electron microscopy, and specific surface area analysis. Then, the calcined calcium/chitosan spheres were used for the transesterification of sunflower oil with methanol. Sunflower seed oil was converted to methyl ester (FAME) under the optimal reaction conditions: 3 wt%; time, 4 h; temperature, 60°C; magnetic stirring (1000 rpm) was 56.12 ± 32% by weight. These results indicate that chitosan can be used as a precursor for the formation of calcium/chitosan spheres to produce porous calcium oxide (with a high surface area) which can be used as an alkaline catalyst for biodiesel production.

Liang et al. [51] prepared a new polymer-based alkaline biodiesel catalyst from epichlorohydrin (ECH)-crosslinked n-[(2-hydroxy-3-trimethylammonium) propyl] chitosan chloride (HTCC) and sodium silicate (Na_2SiO_3). The structure and properties of the catalyst were studied by Fourier-transform infrared spectroscopy, thermogravimetry-mass spectrometry, and transmission electron microscopy. The effects of various factors on the preparation of biodiesel by transesterification of soybean oil were studied. The results show that Na_2SiO_3 is bridged on the HTCC chain by ECH and dispersed in the HTCC matrix in nanoscale. Under the optimum reaction conditions (6/1 methanol/oil mole ratio and 4 wt% catalyst dosage at 55°C for 1 h), a high biodiesel yield of 97.0% was obtained. After the second reaction, the catalyst activity remained stable, which was conducive to the stability and dispersion of Na_2SiO_3 in the catalyst.

Fu et al. [52] used chitosan as a new substrate for immobilization of CaO. Biodiesel was produced by transesterification of soybean oil with methanol, and Cao immobilized on chitosan beads was used as a heterogeneous catalyst. To obtain a stable immobilized catalyst, chitosan beads with immobilized CaO were crosslinked with glutaraldehyde. Two crosslinking parameters, crosslinking time and glutaraldehyde concentration were studied to reveal the optimal immobilization conditions, which were 30 min and 0.22 mol/L^{-1}, respectively. Under those conditions, the immobilized catalyst with a very low CaO leaching rate can be obtained. The immobilized CaO catalyst was prepared by transesterification of soybean oil with methanol. The transesterification rate was studied by response surface

methodology, which was affected by catalyst loading, methanol-oil molar ratio, and temperature. The maximum reaction rate was 0.6 H^{-1}, the molar ratio of methanol to oil was 13.4 at 60°C, and the catalyst loading was 13.78 wt%. Under these conditions, the equilibrium conversion of soybean oil was 97% after 3 hours. In addition, the fixed catalyst can be reused at least five times. This study developed a simple and energy-saving method to prepare chitosan-based immobilized CaO catalyst, which is expected to be used in potential applications including biodiesel production.

5.2. Organic Base. He et al. [53] synthesized guanidine chitosan (GCS) as the heterogeneous basic catalyst for transesterification of soybean oil with methanol using amino methylene sulfonic acid as a graft (in Figure 9). The structure and properties of GCS films were studied by Fourier-transform infrared spectroscopy, thermogravimetric analysis, and X-ray photoelectron spectroscopy. Under the conditions of catalyst dosage of 20%, methanol-oil ratio of 2.5 : 1, reaction temperature of 60°C, and reaction time of 6 h, the conversion of soybean oil reached 98.8% for the first time, and 96.6% for the fifth time. The results showed that the transesterification mainly occurred on the surface of the catalytic membrane. The kinetics of transesterification was studied by a pseudohomogeneous model. The reaction was a first-order reaction with an activation energy of 76.95 kJ/mol and a pre-exponential factor of 7.94×10^9 min^{-1}.

6. Modified Chitosan/Enzyme Catalysts

The unique structure of chitosan is not considered an excellent carrier for immobilized lipase, which promotes the production of a variety of chitosan-loaded lipases. Its advantages include low reaction temperature, repeated use, and high reaction activity. This makes chitosan-loaded lipase widely used in the production of biodiesel.

Rhizopus lipase was immobilized on magnetic chitosan microspheres (MCMs), and biodiesel was prepared from soybean oil and methanol. The maximum content of methyl ester in the reaction mixture reached 91.3 (w/v) at the flow rate of 25 mL/min and the magnetic field strength of 150 Oe. In addition, MCMs-immobilized lipase in the reactor has excellent reusability, and it still maintains 82% productivity even after 6 batches, which is far better than that in a traditional fluidized bed reactor. These results show that MCMs-immobilized lipase is a promising biodiesel production method [54].

The preparation of biodiesel from rapeseed soap residue methanol catalyzed by chitosan-immobilized *Candida* lipase (CRL) was studied by response surface methodology (RSM). Methanol-substrate molar ratio, enzyme dosage, water content, and reaction temperature are four important parameters. RSM analysis shows that the experimental values are in good agreement with the predicted values. The results show that the most effective parameter is water content, which is in good agreement with the experimental values. The coefficient of determination (R2) of the model is 92.86%, with a probability value of $P < 0.0001$. The optimal conditions for biodiesel production by immobilized lipase were as follows: the molar ratio of methanol to the substrate was 4 : 1, the amount of lipase was 8%, the water content was 6%, and the reaction temperature was 45°C. After molecular distillation, the content of methyl ester is more than 95% [55].

Magnetic whole-cell biocatalyst (MWCB) was prepared using chitosan Fe_3O_4 microspheres as a carrier (in Figure 10). The yield of biodiesel was 87.32% after 48 h. After 10 cycles, the yield of biodiesel was 83.57%, which was higher than that of whole-cell biocatalyst without Fe_3O_4 (74.06%). It can be seen that the introduction of magnetic particles not only makes the catalyst easy to separate but also effectively immobilizes the active enzyme to avoid the loss of yield. Interestingly, in previous studies, it was not realized that the introduction of magnetic particles can also increase the yield [56].

Cubides-Roman et al. [57] used magnetic chitosan-immobilized *Pseudomonas fluorescens* lipase as a biocatalyst to study the enzymatic synthesis of ethyl ester from coconut oil and ethanol in an electromagnetic field-assisted bioreactor. The results show that under the conditions of 30°C, 45°C, and 60°C, oil alcohol molar ratios of 1 : 6, 1 : 9, and 1 : 12, and magnetic induction intensity of 6.5, the maximum conversion is about 12%. In the differential reactor, the molar ratio of oil to alcohol was 1 : 11.25, and the reaction time was 12 h In this unconventional bioreactor, under the assistance of a magnetic field, the synthesis of esters is positively affected by the molar ratio and temperature, and magnetic induction is very important for the establishment of a magnetically stabilized bed. In addition, magnetic biocatalysts are retained/separated for further use. Although this interesting device did not obtain a large yield, the application of the new device proved that this model can be used for transesterification to synthesize biodiesel, which added a new method for the preparation of biodiesel.

At present, the efficiency of biomass-based materials is further improved, and the application of immobilized enzymes in biodiesel synthesis is expanded. Batista et al. [58] reported a new biodegradable membrane catalyst, which is composed of chitosan, lipase, and polyvinyl alcohol. The thicknesses of PVA/chitosan and PVA/chitosan/lipase membranes were 70.4 and 79 μm, respectively. The SEM images showed the formation of continuous films without holes or cracks. It is estimated that the lipase rejection efficiency is 92%. The membrane can be reused for 25 hydrolysis cycles and can maintain 62% of the initial activity. These results show that PVA/chitosan/lipase is a promising material for biodiesel production. Similarly, Xie and Wang [25] used magnetic chitosan microspheres to immobilize lipase to study the transesterification of soybean oil. Using glutaraldehyde as a crosslinking agent, magnetic chitosan microspheres lipase was prepared by the chemical coprecipitation method. Using immobilized lipase, the yield of converted soybean oil fatty acid methyl ester reached 87% at an alcohol-oil ratio of 4 : 1, 35°C, and 30 h. the catalyst was reused 4 times without significant reduction inactivity.

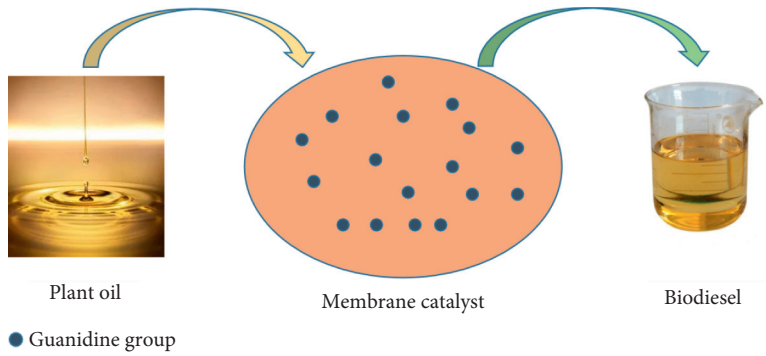

Figure 9: The chitosan-based membrane catalyst. Reproduced with permission from [53] copyright 2015, Elsevier.

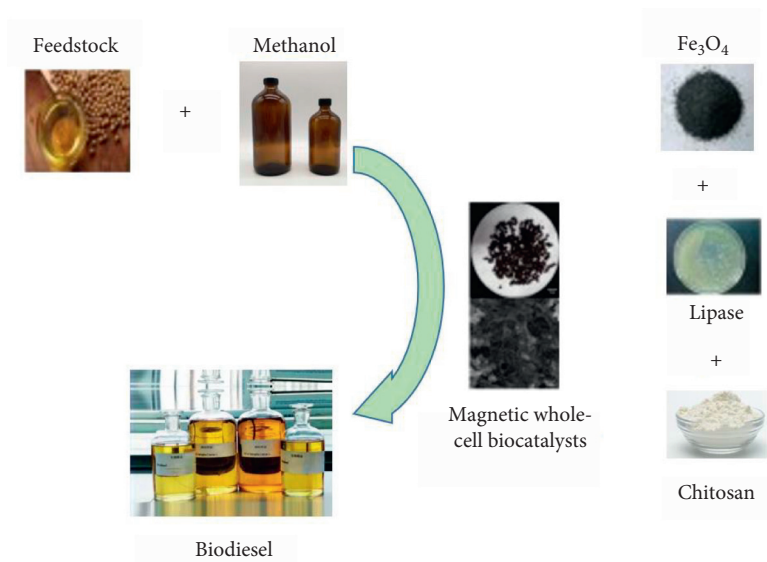

Figure 10: The magnetic chitosan biocatalysts. Reproduced with permission from [56] copyright 2016, Elsevier.

Undoubtedly, lipase can efficiently catalyze transesterification at low temperatures, which is considered to be the greatest advantage of lipase in biodiesel synthesis. However, the high cost of lipase is considered to be the main obstacle to the commercialization of enzymatic transesterification. Karimi synthesized superparamagnetic iron oxide nanoparticles (SPIONs), coated them on silica, and then grafted aldehyde groups to immobilize Bacillus capacity lipase, which is a promising method to improve the economy of enzymatic transesterification. The results show that the average particle size of SPIONs is about 20 nm. The nanoparticles linked to lipase showed almost superparamagnetism. Under the conditions of methanol to oil molar ratio of 6 : 1, immobilized lipase concentration of 25%, n-hexane content of 10%, the water content of 10%, reaction temperature at 35°C, and reaction time of 35 h, the conversion rate of WCO to biodiesel reached 91%. The immobilized lipase is easy to recover and reuse, and the enzyme activity has hardly decreased [59].

Chitosan was tried to be used as a perfect carrier for lipase immobilization by adsorption and crosslinking. The immobilization efficiency of the crosslinking method was 99.1%, and the reusability was 12 cycles. The esterification of oleic acid and transesterification of olive oil showed that the partially purified enzyme proved its ability to catalyze the formation of methyl oleate. The partially purified and immobilized lipase of *Rhizopus oryzae* R1 has excellent efficiency and reusability and plays an important role in biodiesel production [60].

7. Conclusions

This paper reviews the application of heterogeneous catalysts supported on biomass-based chitosan in the synthesis of biodiesel. Chitosan has the greatest advantage of having a large number of active amino and hydroxyl groups, easy to modify and graft, and easy to chelate metal ions. At the same time, it can be compounded with a variety of materials to obtain multifunctional catalytic materials, which will undoubtedly improve the catalytic efficiency. At present, it is common to prepare chitosan-based catalysts rich in acid, alkali, metal ions, or enzyme active sites. However, these

catalysts with different forms still have the problems of low catalyst surface area, easy loss of active centers, and difficult separation, and there is still a need for further improvement.

Therefore, we need to further develop new chitosan-based materials to make this kind of catalyst not only to have good catalytic efficiency but also biodegradable, green, and nontoxic and can be used many times. At present, the number of chitosan-based biodiesel synthesis materials reported is limited. It is hoped that more chitosan-based catalysts with excellent performance can be developed and applied to the large-scale production of biodiesel based on laboratory research.

Data Availability

No data were used in the study.

Conflicts of Interest

The authors declare no conflicts of interest.

Acknowledgments

This study was financially supported by the Guizhou Science and Technology Foundation ([2021]075) and Guizhou Provincial Characteristic Key Laboratory (QJHKY [2021] 002).

References

[1] R. V. Quah, Q. Yie, H. Tan et al., "An overview of biodiesel production using recyclable biomass and nonbiomass derived magnetic catalysts," *Journal of Environmental Chemical Engineering*, vol. 7, no. 4, Article ID 103219, 2019.

[2] H. Zhang, H. Li, C. C. Xu, and S. Yang, "Heterogeneously chemo/enzyme-functionalized porous polymeric catalysts of high-performance for efficient biodiesel production," *ACS Catalysis*, vol. 9, no. 12, pp. 10990–11029, 2019.

[3] M. R. Avhad and J. M. Marchetti, "Innovation in solid heterogeneous catalysis for the generation of economically viable and eco-friendly biodiesel: a review," *Catalysis Reviews*, vol. 58, no. 2, pp. 157–208, 2016.

[4] Z.-E. Tang, S. Lim, Y.-L. Pang, H.-C. Ong, and K.-T. Lee, "Synthesis of biomass as heterogeneous catalyst for application in biodiesel production: state of the art and fundamental review," *Renewable and Sustainable Energy Reviews*, vol. 92, pp. 235–253, 2018.

[5] N. Mansir, Y. H. Taufiq-Yap, U. Rashid, and I. M. Lokman, "Investigation of heterogeneous solid acid catalyst performance on low-grade feedstocks for biodiesel production: a review," *Energy Conversion and Management*, vol. 141, pp. 171–182, 2017.

[6] R. Wang, M. A. Hanna, W.-W. Zhou et al., "Production and selected fuel properties of biodiesel from promising non-edible oils: *Euphorbia lathyris L.*, *Sapium sebiferum L.* and *Jatropha curcas L*," *Bioresource Technology*, vol. 102, no. 2, pp. 1194–1199, 2011.

[7] F. Chang, M. A. Hanna, D.-J. Zhang et al., "Production of biodiesel from non-edible herbaceous vegetable oil: *Xanthium Sibiricum* patr," *Bioresource Technology*, vol. 140, pp. 435–438, 2013.

[8] H. Zhang, H. Li, H. Pan et al., "Efficient production of biodiesel with promising fuel properties from *Koelreuteria integrifoliola* oil using a magnetically recyclable acidic ionic liquid," *Energy Conversion and Management*, vol. 138, pp. 45–53, 2017.

[9] H. Zhang, Q. Zhou, F. Chang et al., "Production and fuel properties of biodiesel from *Firmiana platanifolia L.f.* as a potential non-food oil source," *Industrial Crops and Products*, vol. 76, pp. 768–771, 2015.

[10] M. Kirubakaran and V. Arul Mozhi Selvan, "A comprehensive review of low cost biodiesel production from waste chicken fat," *Renewable and Sustainable Energy Reviews*, vol. 82, pp. 390–401, 2018.

[11] A. F. Lee, J. A. Bennett, J. C. Manayil, and K. Wilson, "Heterogeneous catalysis for sustainable biodiesel productionviaesterification and transesterification," *Chemical Society Reviews*, vol. 43, no. 22, pp. 7887–7916, 2014.

[12] N. Narkhede, S. Singh, and A. Patel, "Recent progress on supported polyoxometalates for biodiesel synthesis via esterification and transesterification," *Green Chemistry*, vol. 17, no. 1, pp. 89–107, 2015.

[13] B. S. Sazzad, M. A. Fazal, A. S. M. A. Haseeb, and H. H. Masjuki, "Retardation of oxidation and material degradation in biodiesel: a review," *RSC Advances*, vol. 6, no. 65, pp. 60244–60263, 2016.

[14] I. M. Atadashi, M. K. Aroua, A. R. A. Aziz, and N. M. N. Sulaiman, "Production of biodiesel using high free fatty acid feedstocks," *Renewable & Sustainable Energy Reviews*, vol. 16, no. 5, pp. 3275–3285, 2018.

[15] A. Marwaha, A. Dhir, S. K. Mahla, and S. K. Mohapatra, "An overview of solid base heterogeneous catalysts for biodiesel production," *Catalysis Reviews*, vol. 60, no. 4, pp. 594–628, 2018.

[16] A. Guldhe, B. Singh, T. Mutanda, K. Permaul, and F. Bux, "Advances in the synthesis of biodiesel via enzyme catalysis: novel and sustainable approaches," *Renewable and Sustainable Energy Reviews*, vol. 41, pp. 1447–1464, 2015.

[17] F. Zhang, X.-H. Wu, M. Yao, Z. Fang, and Y.-T. Wang, "Production of biodiesel and hydrogen from plant oil catalyzed by magnetic carbon-supported nickel and sodium silicate," *Green Chemistry*, vol. 18, no. 11, pp. 3302–3314, 2016.

[18] B. Yang, L. Leclercq, J.-M. Clacens, and V. Nardello-Rataj, "Acidic/amphiphilic silica nanoparticles: new eco-friendly pickering interfacial catalysis for biodiesel production," *Green Chemistry*, vol. 19, no. 19, pp. 4552–4562, 2017.

[19] A. Wang, H. Li, H. Zhang, H. Pan, and S. Yang, "Efficient catalytic production of biodiesel with acid-base bifunctional rod-like Ca-B oxides by the sol-gel approach," *Materials*, vol. 12, no. 1, p. 83, 2019.

[20] A. Hykkerud and J. M. Marchetti, "Esterification of oleic acid with ethanol in the presence of Amberlyst 15," *Biomass and Bioenergy*, vol. 95, pp. 340–343, 2016.

[21] H. Zhang, L.-L. Zhang, X. Tan, H. Li, and S. Yang, "Catalytic high-yield biodiesel production from fatty acids and non-food oils over a magnetically separable acid nanosphere," *Industrial Crops and Products*, vol. 173, Article ID 114126, 2021.

[22] A. Wang, P. Sudarsanam, Y. Xu, H. Zhang, H. Li, and S. Yang, "Functionalized magnetic nanosized materials for efficient biodiesel synthesis via acid-base/enzyme catalysis," *Green Chemistry*, vol. 22, no. 10, pp. 2977–3012, 2020.

[23] S. H. Y. S. Abdullah, N. H. M. Hanapi, A. Azid et al., "A review of biomass-derived heterogeneous catalyst for a sustainable biodiesel production," *Renewable and Sustainable Energy Reviews*, vol. 70, pp. 1040–1051, 2017.

[24] Y.-K. Lin, V.-H. Nguyen, J. C.-C. Yu et al., "Biodiesel production by pervaporation-assisted esterification and pre-esterification using graphene oxide/chitosan composite membranes," *Journal of the Taiwan Institute of Chemical Engineers*, vol. 79, pp. 23–30, 2017.

[25] W. Xie and J. Wang, "Immobilized lipase on magnetic chitosan microspheres for transesterification of soybean oil," *Biomass and Bioenergy*, vol. 36, pp. 373–380, 2012.

[26] P. A. Russo, M. M. Antunes, P. P. Neves et al., "Mesoporous carbon–silica solid acid catalysts for producing useful bio-products within the sugar-platform of biorefineries," *Green Chemistry*, vol. 16, no. 9, pp. 4292–4305, 2014.

[27] X. Li, K. Cui, Z. Guo et al., "Heterogeneous Fenton-like degradation of tetracyclines using porous magnetic chitosan microspheres as an efficient catalyst compared with two preparation methods," *Chemical Engineering Journal*, vol. 379, Article ID 122324, 2020.

[28] A. Dhakshinamoorthy, M. Jacob, N. S. Vignesh, and P. Varalakshmi, "Pristine and modified chitosan as solid catalysts for catalysis and biodiesel production: a minireview," *International Journal of Biological Macromolecules*, vol. 167, pp. 807–833, 2021.

[29] Z. Yao, C. Zhang, Q. Ping, and L. Yu, "A series of novel chitosan derivatives: synthesis, characterization and micellar solubilization of paclitaxel," *Carbohydrate Polymers*, vol. 68, no. 4, pp. 781–792, 2007.

[30] X.-N. Zhao, G.-F. Hu, M. Tang et al., "A highly efficient and recyclable cobalt ferrite chitosan sulfonic acid magnetic nanoparticle for one-pot, four-component synthesis of 2H-indazolo[2,1-b] phthalazine -triones," *RSC Advances*, vol. 4, no. 93, pp. 51089–51097, 2014.

[31] Y. Xiang, M. Yang, Z. Guo, and Z. Cui, "Alternatively chitosan sulfate blending membrane as methanol-blocking polymer electrolyte membrane for direct methanol fuel cell," *Journal of Membrane Science*, vol. 337, no. 1-2, pp. 318–323, 2009.

[32] L. Gu, Z. Zhang, S. Yang et al., "Chitosan-modified polyvinyl alcohol membrane high performance in biodiesel/methanol pervaporation separation," *ChemistrySelect*, vol. 6, no. 34, pp. 9052–9059, 2021.

[33] K. C. Gupta and F. H. Jabrail, "Glutaraldehyde cross-linked chitosan microspheres for controlled release of centchroman," *Carbohydrate Research*, vol. 342, no. 15, pp. 2244–2252, 2007.

[34] Y. Liu, S. Jia, Q. Wu, J. Ran, W. Zhang, and S. Wu, "Studies of Fe_3O_4-chitosan nanoparticles prepared by co-precipitation under the magnetic field for lipase immobilization," *Catalysis Communications*, vol. 12, no. 8, pp. 717–720, 2011.

[35] J. Li, C. Zhang, P. Jiang, and Y. Leng, "Cross-linked chitosan supporting polyoxometalates catalyst with adjustable redox property for H_2O_2-based oxidation reactions," *Catalysis Communications*, vol. 94, pp. 13–17, 2017.

[36] R. Bodmeier, H. Chen, and O. Paeratakul, "Novel approach to the oral delivery of micro-or nanoparticles," *Pharmaceutical Research*, vol. 6, no. 5, pp. 413–417, 1989.

[37] J. Huang, Y. Liang, H. Hu et al., "Ultrahigh-surface-area hierarchical porous carbon from chitosan: acetic acid mediated efficient synthesis and its application in superior supercapacitors," *Journal of Materials Chemistry A*, vol. 5, no. 47, pp. 24775–24781, 2017.

[38] B. Sahoo, A.-E. Surkus, M.-M. Pohl et al., "A biomass-derived non-noble cobalt catalyst for selective hydrodehalogenation of alkyl and (hetero) aryl halides," *Angewandte Chemie International Edition*, vol. 56, no. 37, pp. 11242–11247, 2017.

[39] J. Roosen, J. Spooren, and K. Binnemans, "Adsorption performance of functionalized chitosan–silica hybrid materials toward rare earths," *Journal of Materials Chemistry A*, vol. 2, no. 45, pp. 19415–19426, 2014.

[40] F. Sana, P. Ana, and L. Mohamed, "Pd embedded in chitosan microspheres as tunable soft-materials for sonogashira cross-coupling in the water-ethanol mixture," *Green Chemistry*, vol. 17, pp. 1893–1898, 2015.

[41] H. Kayser, F. Pienkoß, and P. Domínguez de María, "Chitosan catalyzed biodiesel synthesis: proof-of-concept and limitations," *Fuel*, vol. 116, pp. 267–272, 2014.

[42] R. B. da Silva, A. F. Lima Neto, L. S. Soares dos Santos et al., "Catalysts of Cu (II) and Co (II) ions adsorbed in chitosan used in transesterification of soybean and babassu oils–a new route for biodiesel syntheses," *Bioresource Technology*, vol. 99, no. 15, pp. 6793–6798, 2008.

[43] N. Saengprachum, D. Cai, M. Li, L. Li, X. Lin, and T. Qiu, "Acidic chitosan membrane as an efficient catalyst for biodiesel production from oleic acid," *Renewable Energy*, vol. 143, pp. 1488–1499, 2019.

[44] C. S. Caetano, M. Caiado, J. Farinha et al., "Esterification of free fatty acids over chitosan with sulfonic acid groups," *Chemical Engineering Journal*, vol. 230, pp. 567–572, 2013.

[45] A. Wang, H. Zhang, H. Li, and S. Yang, "Efficient production of methyl oleate using a biomass-based solid polymeric catalyst with high acid density," *Advances in Polymer Technology*, vol. 2019, Article ID 4041631, 11 pages, 2019.

[46] T. Tong, Y. Li, R. Hou, X. Wang, and S. Wang, "Decoration of chitosan microspheres with brønsted heteropolyacids and lewis ion Ti: trifunctional catalysts for esterification to biodiesel," *RSC Advances*, vol. 7, no. 67, pp. 42422–42429, 2017.

[47] X.-X. Han, K.-K. Chen, W. Yan et al., "Amino acid-functionalized heteropolyacids as efficient and recyclable catalysts for esterification of palmitic acid to biodiesel," *Fuel*, vol. 165, pp. 115–122, 2016.

[48] A. Wang, H. Li, H. Pan et al., "Efficient and green production of biodiesel catalyzed by recyclable biomass-derived magnetic acids," *Fuel Processing Technology*, vol. 181, pp. 259–267, 2018.

[49] L. Fereidooni and M. Mehrpooya, "Experimental assessment of electrolysis method in the production of biodiesel from waste cooking oil using zeolite/chitosan catalyst with a focus on waste biorefinery," *Energy Conversion and Management*, vol. 147, pp. 145–154, 2017.

[50] L. M. Correia, N. D. S. Campelo, R. D. F. Albuquerque et al., "Calcium/chitosan spheres as catalyst for biodiesel production," *Polymer International*, vol. 64, no. 2, pp. 242–249, 2015.

[51] M. Liang, B. He, Y. Shao, J. Li, and Y. Cheng, "Preparation and catalytic performance of N-[(2-Hydroxy-3-trimethylammonium)propyl] chitosan chloride/Na_2SiO_3 polymer-based catalyst for biodiesel production," *Renewable Energy*, vol. 88, pp. 51–57, 2016.

[52] C.-C. Fu, T.-C. Hung, C.-H. Su et al., "Immobilization of calcium oxide onto chitosan beads as a heterogeneous catalyst for biodiesel production," *Polymer International*, vol. 60, no. 6, pp. 957–962, 2011.

[53] B. He, Y. Shao, M. Liang, J. Li, and Y. Cheng, "Biodiesel production from soybean oil by guanidinylated chitosan," *Fuel*, vol. 159, pp. 33–39, 2015.

[54] G.-X. Zhou, G.-Y. Chen, and B.-B. Yan, "Biodiesel production in a magnetically-stabilized, fluidized bed reactor with an immobilized lipase in magnetic chitosan microspheres," *Biotechnology Letters*, vol. 36, no. 1, pp. 63–68, 2014.

[55] P. Shao, X. Meng, J. He, and P. Sun, "Analysis of immobilized candida rugosa lipase-catalyzed preparation of biodiesel from

rapeseed soapstock," *Food and Bioproducts Processing*, vol. 86, no. 4, pp. 283–289, 2008.

[56] G. Chen, J. Liu, Y. Qi, J. Yao, and B. Yan, "Biodiesel production using magnetic whole-cell biocatalysts by immobilization of pseudomonas mendocina on Fe_3O_4-chitosan microspheres," *Biochemical Engineering Journal*, vol. 113, pp. 86–92, 2016.

[57] D. C. Cubides-Roman, V. H. Pérez, H. F. de Castro et al., "Ethyl esters(biodiesel) production by pseudomonas fluorescens lipase immobilized on chitosan with magnetic properties in a bioreactor assisted byelectromagnetic field," *Fuel*, vol. 196, pp. 481–487, 2017.

[58] K. A. Batista, F. M. Lopes, F. Yamashita, and K. F. Fernandes, "Lipase entrapment in PVA/chitosan biodegradable film for reactor coatings," *Materials Science and Engineering: C*, vol. 33, no. 3, pp. 1696–1701, 2013.

[59] M. Karimi, "Immobilization of lipase onto mesoporous magnetic nanoparticles for enzymatic synthesis of biodiesel," *Biocatalysis and Agricultural Biotechnology*, vol. 8, pp. 182–188, 2016.

[60] S. E. Helal, H. M. Abdelhady, K. A. Abou-Taleb, M. G. Hassan, and M. M. Amer, "Lipase from rhizopus oryzae R1: in-depth characterization, immobilization, and evaluation in biodiesel production," *Journal of Genetic Engineering and Biotechnology*, vol. 19, no. 1, pp. 1–13, 2021.

Hindawi
International Journal of Chemical Engineering
Volume 2021, Article ID 4630661, 8 pages
https://doi.org/10.1155/2021/4630661

Research Article

Effect of Nitrogen Ion Implantation Energy on the Mechanical and Chemical Properties of AISI M50 Steel

Xiangyu Xie,[1] Chao Chen,[2] Jun Luo,[1] and Jin Xu[2]

[1]*Guizhou Provincial College-based Engineering Research Center for Materials Protection of Wear and Corrosion, College of Chemistry and Materials Engineering, Guiyang University, Guiyang 550005, China*
[2]*School of Mechanical Engineering, Guizhou University, Guiyang 550000, China*

Correspondence should be addressed to Jun Luo; luojun_gyu@sina.com

Received 10 June 2021; Revised 14 July 2021; Accepted 11 September 2021; Published 12 October 2021

Academic Editor: Valeria Di Sarli

Nitrogen ion implantation has shown its role in enhancing steel surface properties. In this work, AISI M50 steel was implanted with nitrogen ions by using the metal vapor vacuum arc technique with a dose of 2×10^{17} cm^{-2}, and corresponding implanted energies were at 60 keV, 80 keV, and 100 keV, respectively. The distribution of implanted nitrogen ions was calculated, and the samples were tribologically tested and examined. As shown by the results, the microhardness in implanted samples was 1.17 times greater relative to that of the unimplanted sample. The implantation of the nitrogen ion leads to a change in the friction coefficient of the AISI M50 steel. Adhesive wear mechanism occurs in the unimplanted sample, and adhesion resistance tends to increase when nitrogen-implanted energy increases. The formation of oxides α-Fe_2O_3 and Fe_3O_4 further enhanced the tribological properties for implanted samples.

1. Introduction

Bearing, as an integral part in various mechanical equipment, is critical for equipment performance, level, quality, and reliability of the equipment [1]. Advance of science and technology has stimulated greater demands for bearing materials, which possess reinforced performance and applicability to harsh environments [2]. As a representative metal material marked by favorable mechanical properties, AISI M50 steel has been extensively adopted by the production for aerobearings [3]. AISI M50 steel is often subjected to continuous heavy loads and high speeds, and in these harsh environments, the material surface can undergo a variety of failure behaviours, such as damage, wear, and plastic deformation [4]. In order to reinforce the surface properties and wear resistance for the steel, many surface treatment methods have been proposed. It is a feasible choice to use surface modification technology for the improvement of steel surface properties. Compared to other surface techniques, such as chemical heat treatment [5], laser melting [6], and chemical etching [7], ion implantation possesses higher precision and a cleaner environment [8]. Ion implantation can easily create a progressive interface between the implanted surface layer and the unaffected material volume, without altering the dimension of original materials. Ion implantation technique triggers variations in the material surface and chemical composition, including microstructure [9], chemical properties [10], and biological properties [11].

According to former studies, the implantation of nitrogen ions and other kinds of ions into specific steels can improve mechanical and tribological properties, especially hardness, and this has a connection with wear resistance [12–15]. Moreover, ion implantation is used for different metallic materials and acts beneficially for preventing from another unique form of damage likewise cavitation erosion [16, 17]. So far, few studies concentrate on the surface modifications in AISI M50 steel with ion implantation, in particular nitrogen ion implantation. Multiple factors may exert influence on the treated surface's ultimate quality, including the implanted energy, type of ions, and doses [18, 19]. However, much attention

has been paid to the assessment about AISI M50 steel surface properties under various implantation conditions, especially the implanted energy. The research implanted nitrogen ions containing various energies into the AISI M50 steel surface and reported the improvement in surface properties, thus providing valuable references for industrial applications.

2. Materials and Methods

2.1. Experimental Sample. AISI M50 steel was used as a metal substrate in the formation of form C: 0.82 wt.%, Cr: 4.00 wt.%, Mo: 4.25 wt.%, V: 1.10 wt.%, Mn: 0.16 wt.%, Si: 0.13 wt.%, and Ni: 0.07 wt.%, balanced with Fe. Prior to nitrogen ion implantation, AISI M50 steel was cut into flat samples with a dimension of 30 mm × 20 mm × 10 mm and then polished by silicon carbide emery papers of 120, 400, 800, and 1200 grit. The last polishing was made with 3.5 μm and 1 μm diamond pastes to a mirror finish with a roughness of *Ra* approx. 0.05 μm. All samples were cleaned ultrasonically with acetone and dried.

2.2. Ion Implantation Method. The implantation samples were implanted with the MEVVA (metal vapor vacuum arc) source implanter at the Key Laboratory of Beam Technology and Material Modification of Ministry of Education, Beijing. Nitrogen ions were implanted at a dose of 2×10^{17} cm^{-2} under normal ambient temperature, and implantation energies were implanted with three fluences: 60 keV, 80 keV, and 100 keV.

2.3. Properties of the Nitrogen Ion-Implanted Layers. To investigate the distribution and range of implanted ions, Monte Carlo simulation program (SRIM-2013 package) was used to make predictions. The density of target AISI M50 steel was set to 7.865 g/cm^3, and the number of total nitrogen ions for calculations was set to 2,000,000. X-ray photoelectron spectroscopy (XPS) analysis was conducted using Thermo Fisher Scientific K-Alpha+ for determining the surface. The microhardness indentations were conducted under the HXS-1000AK hardness tester with a load of 10 g for 10 s, and each sample was indented at five different locations to calculate average hardness.

2.4. Friction Test and Surface Characterization. Friction and wear were calculated under technically dry friction conditions. A tribological experiment proceeded on a roller-on-flat configuration with the UMT TriboLab device of Bruker Corporation. In this test, AISI M50 steel flat slid against a roller (M50 steel) of Φ12 × 12 mm in diameter and a hardness of 710 HV. 1 Hz test oscillating frequency and a constant load of 30 N were adopted in this test. The track length reached 2.4 mm, and the test lasted for 0.5 h, and each test was repeated three times. Surface chemical state was detected using the DXR^{TM} Raman spectrometer, with a wavelength of 514.5 nm laser served as an excitation source, and its power was set to 5 mW. Worn surface morphology was checked using FEI Quanta 250 scanning electron microscopy. The cross section for the wear track was determined by the Contour GT-K surface profiler of Bruker Corporation.

3. Results and Discussion

3.1. Distribution of Implanted Ions. The theoretical distribution of implanted ions arising from implantation on sample depth was measured using SRIM software [20]. In comparison with lower energy, higher energy induces the migration of peak nitrogen concentration to the inside of the substrate (Figure 1). The range and depth distribution results of implanted ions are presented in Figure 2. As indicated by the results, the calculated range of implanted nitrogen ions does not exceed 2.0 μm, and the maximum concentration of the gap can be noted at the depth of around 1.0 μm. With different implantation energies, the implantation depth increases with energy. According to the LSS theory (Lindhard, Scharff, and Schiott) [21], implantation depth depends on the ions' energy, i.e., the higher the ion energy, the higher the implantation depth. These calculated results are highly consistent with the LSS theory.

Figures 3(a) and 3(b) show the surface N 1s and Cr 2p core spectra in nitrogen ion-implanted samples. According to Figure 3(a), the intense peak near 397.4 eV is ascribed to metal nitrides, such as Fe_xN. As presented in Figure 3(b), the intense peaks near 583.5 eV and 573.8 eV are possibly caused by the chromium compound. The peak at 574.9 eV stands for the Cr_2N phase. This is in good agreement with literature findings [22]. The results of N 1s and Cr 2p spectra further confirmed the formation of the nitride phase on the surface after nitrogen ion implantation.

3.2. Mechanical Properties. The microhardness in unimplanted samples and nitrogen ion-implanted samples can be seen from Figure 4. The microhardness of implanted samples under 10 g load far exceeds that of unimplanted samples. The microhardness in nitrogen ion-implanted samples reduces with the increase of energy. As shown in the family of hardness graphs, the hardness in the unimplanted AISI M50 steel sample is 707 HV, and the nitrogen ion-implanted sample (60 keV) shows the maximum hardness of 830 HV. In contrast to unimplanted samples, the increase approximately reaches 17%. Nitrogen ion-implanted samples are shown to have a hardness of 920 HV. In contrast to unimplanted samples, the increase approximately reaches 30%. The aforementioned hardness-related findings reveal the concurrent increasing trend between hardness and implantation energy of nitrogen ions, indicating that a harder region has formed near the surface. The microhardness results confirm XPS results, confirming element concentration distribution along depth with SRIM. Interstitial nitride phase can effectively strengthen the matrix and improve the hardness.

3.3. Tribological Behavior. Figure 5 presents the friction coefficient curve related to four samples. Obviously, the friction coefficient in unimplanted samples quickly grows to

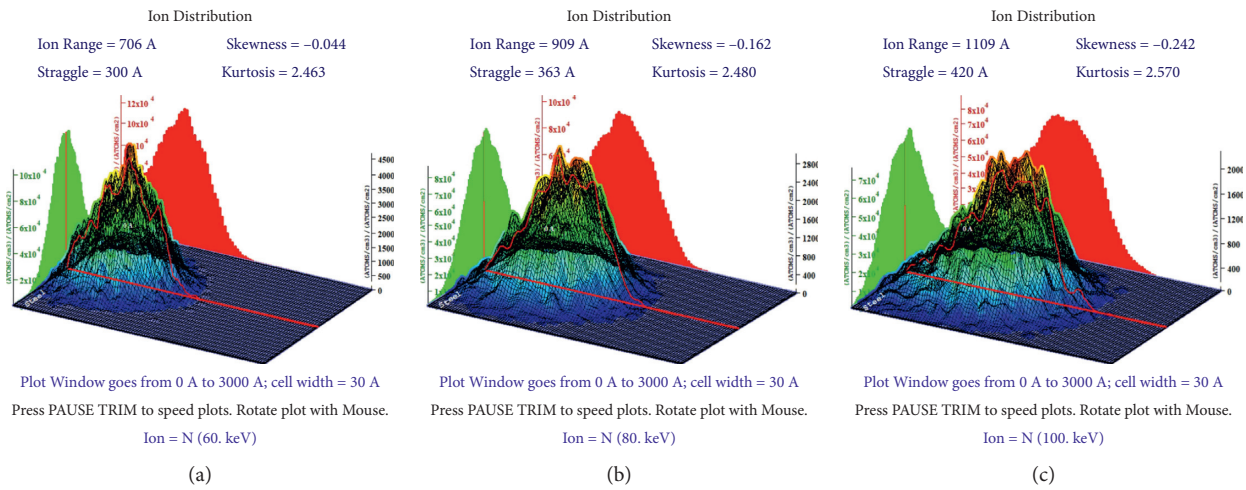

Figure 1: SRIM software simulations for nitrogen profiles of the implanted sample. (a) 60 keV. (b) 80 keV. (c) 100 keV.

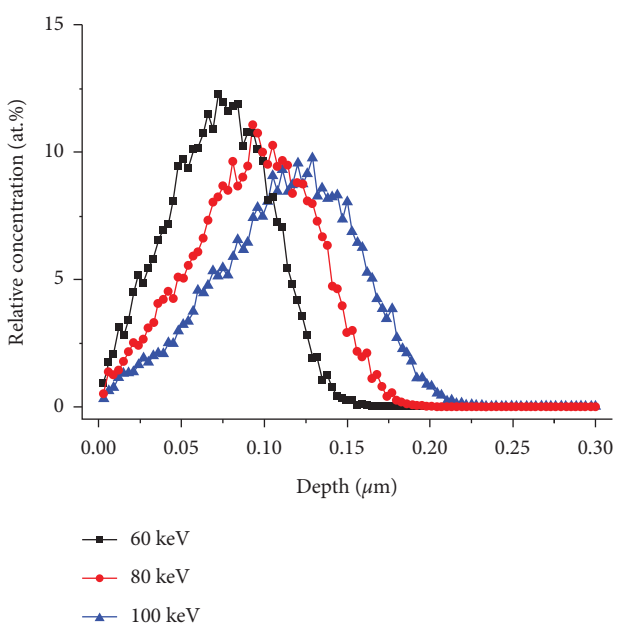

Figure 2: Theoretical distribution of implanted nitrogen ions performed at the energy 60 keV, 80 keV, and 100 keV into the AISI M50 steel.

around 0.5, primarily due to the loss at the surface oxide layer and adsorption layer (Figure 5(a)), whereas the friction coefficient shows a stable trend in the following experimental processes (steady state). It indicates the wide rubbing and poor wear resistance in unimplanted samples. By contrast, in case that nitrogen ion-implanted samples are at 60 keV, the friction process will maintain its stability in the first 70 cycles and subsequently deteriorate quickly, indicating that wear life of samples at 60 keV energy is ~70 cycles. Furthermore, in case that nitrogen ion-implanted samples are at 80 keV energy, a similar friction process can be found, and corresponding sample wear life is 140 cycles. For samples at 100 keV energy, friction coefficient will increase slowly to a similar level, and sample wear life is 320 cycles. The improvement for samples at 100 keV was four times as much as that of samples at 60 keV. Interestingly, despite the similarity between unimplanted and implanted samples in the stability friction coefficient, the friction curve at certain stages is not smooth, showing that the impact of implantation and following interactions and relationships with material properties such as wear is rather complicated, and more investigations should be performed. Mean values of the steady state in friction coefficients of the samples are shown in Figure 5(b). The unimplanted sample exhibited high friction coefficients. With nitrogen ion implantation, the samples presented a lower friction coefficient. The mean values of steady friction coefficients of nitrogen ion-implanted samples reduced as energy increased. These results indicate that the wear life in nitrogen ion-implanted samples in the friction experiment is greatly extended.

Wear tracks were examined by the surface profiler (Figure 6) and scanning electron microscopy (Figure 7). The wear depth of the unimplanted sample was obviously deeper than that of the nitrogen ion-implanted samples on worn scars of AISI M50 steel. From the worn surface, there are many grooves and peelings on the surface of unimplanted samples in the sliding direction (Figure 7(a)). The presence of a plastic deformation zone at the bottom suggests the removal of metal partially. For the implanted sample at 60 keV, some microgrooves and slight cracking can be observed from worn scars. Meanwhile, plastic deformation is weakened (Figure 7(b)). For the implanted sample at 60 keV, there are few pits and peelings on the worn surface (Figure 7(c)). For the nitrogen ion-implanted sample at 100 keV energy, the wear tracks become smooth (Figure 7(d)).

Figure 8 demonstrates the cross section of wear track profiles for unimplanted samples, with a large wear depth. Track depth for ion implantation is more irregular. The wear area is remarkably lessened among nitrogen ion-implanted samples. It was further demonstrated that nitrogen ion implantation might effectively alleviate the wear loss on the AISI M50 steel surface. The obtained profiles for

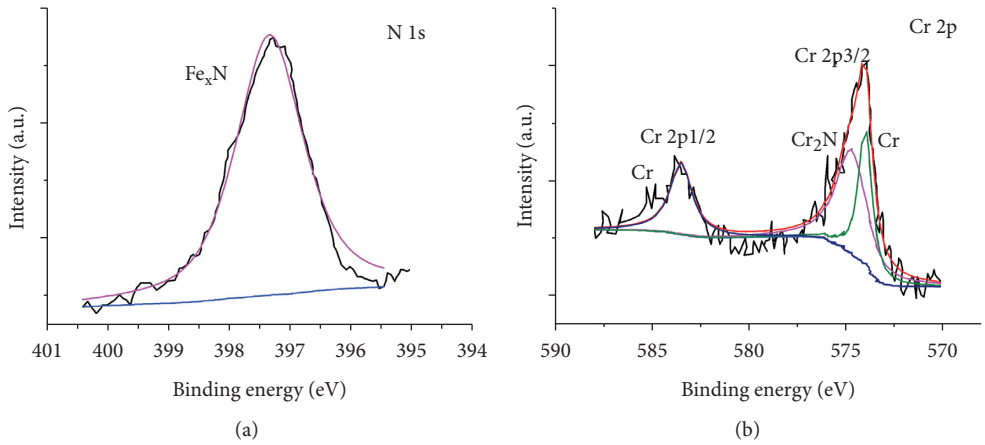

Figure 3: High-resolution XPS spectra of the nitrogen ion-implanted sample. (a) N 1s. (b) Cr 2p.

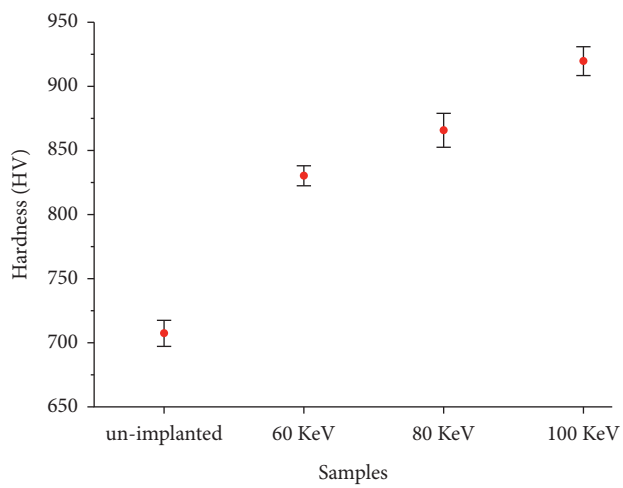

Figure 4: Microhardness of samples after nitrogen ion implantation with different energies.

individual sliding tracks fit the microscopic observational results. The wear track shape of unimplanted and nitrogen ion-implanted samples confirms the existence of grooves and wear particles. As is known, material transfer between contacting surfaces will occur during sliding contact, in particular under dry friction conditions. The results show the similarity between unimplanted samples and implanted samples in wear mechanism. A well-known fact is that the steel surface is subject to both adhesive wear and abrasive wear. Adhesive wear arises from the high pressure during individual contact of asperities, which leads to local adhesion, and such contact is later sheared to form junctions [23]. Relative sliding between contact surfaces leads to rupture in the junctions and frequent transfer of material from one surface to the other. As damage increased, adhesion potentially causes scuffing. It can be ascribed to a large increase in friction coefficient. Depending on the simple operating conditions and the elements of the tribosystem, a single wear mechanism possibly plays a dominant role [24]. As mentioned above, adhesion has to be expected as the dominating wear mechanism of those samples. With nitrogen ion implantation, the wear mechanism still belonged to adhesive wear. However, adhesion resistance shows a trend of increase with nitrogen-implanted energy since abrasion resistance will increase when the hardness of wearing material is greater than that in countersamples.

3.4. Raman Spectroscopy of Wear Scars. Raman spectra measurements are made for detecting different phases collected from both unimplanted and implanted AISI M50 steel surfaces after tribological tests. As seen from Figure 9, several oxide phases' features could be seen from the Raman spectra on worn surfaces. They might be attributed to the tribo-caused oxidation on the surface. Some published works suggest that α-Fe_2O_3 comes under the R-3c crystal space group, and seven phonon lines may emerge in the Raman spectrum, including two A_{1g} phonon modes and five E_g phonon modes [25, 26]. Peaks at 227 and 494 cm^{-1} have a connection with the A_{1g} phonon mode, and peaks at 245, 292, 299, 409, and 609 cm^{-1} are associated with the E_g phonon mode. Thus, it can be seen that the wear product is α-Fe_2O_3. Comparatively, softer phase for oxides such as

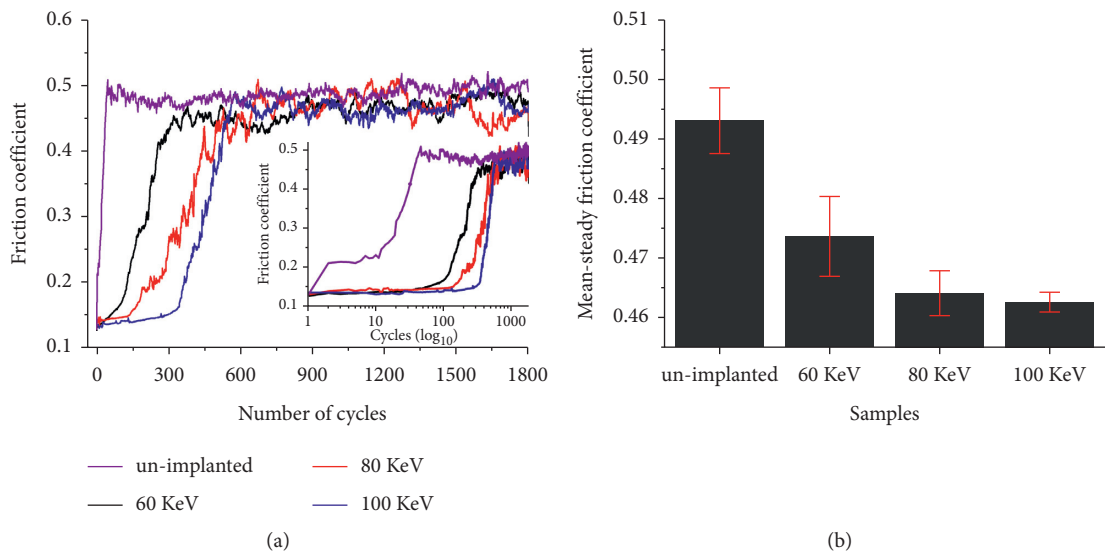

Figure 5: Friction coefficient of unimplanted and nitrogen ion-implanted samples at various energies. (a) The whole test process. (b) Mean values of the steady state.

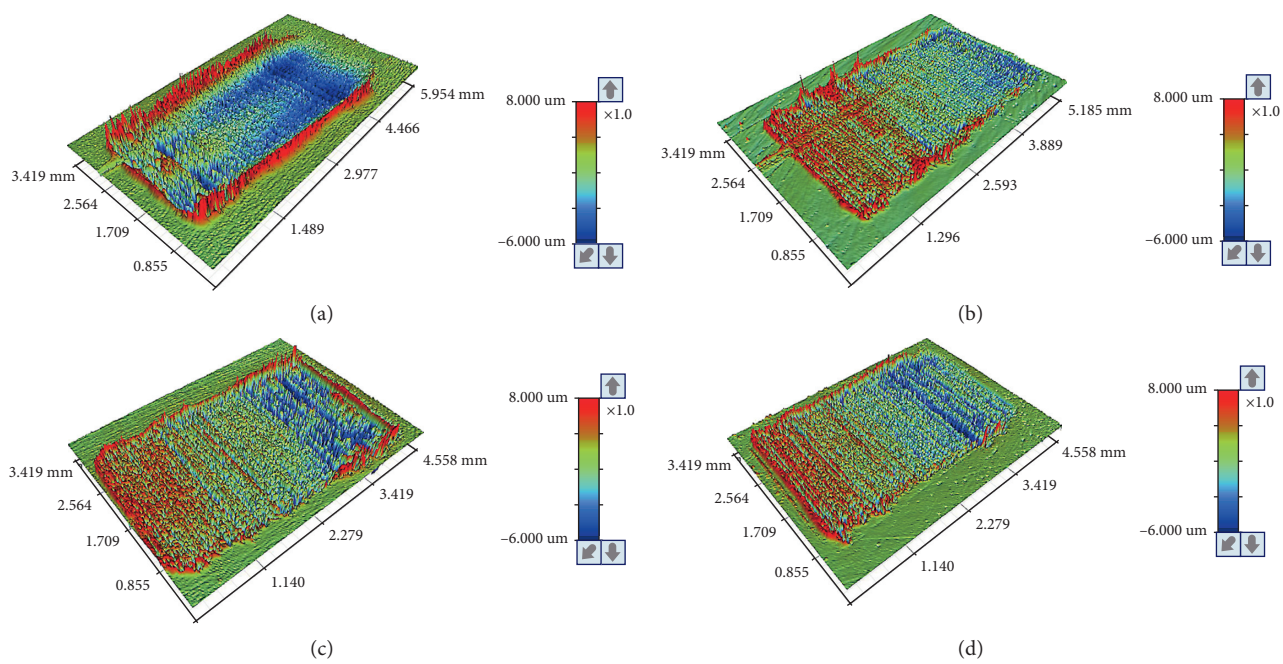

Figure 6: 3D optical profilometer images of the wear tracks for the different implanted energies studied after wear tests. (a) Unimplanted. (b) 60 keV. (c) 80 keV. (d) 100 keV.

α-Fe_2O_3 may take shape during initial sliding stages with a low formation temperature. A peak at 680 cm^{-1} appeared in the Raman spectrum of the implanted sample, indicating the presence of Fe_3O_4, and no similar phenomenon could be seen from wear tracks on unimplanted surfaces. Raman bands at 366 cm^{-1} at a lower nitrogen ion energy belong to the α-Fe_2N phase [27].

Lots of scholars indicated that tribo-oxide layers were efficient in decreasing wear, and Fe_3O_4 produced more protective layers compared with Fe_2O_3 [28]. Oxides α-Fe_2O_3 and Fe_3O_4 reinforce sliding resistance, which leads to the stability of friction, as seen from Figure 5. Such metallic oxides constitute adhesive bonding between interfaces and thus influence the sliding movement. Therefore, a conclusion can be drawn that nitrogen ion implantation treatment promoted the wear resistance for the substrate. Nitride phases harden the surface and have a low shearing factor, which helps reduce friction and reinforce wear resistance. In the meanwhile, consistent with the expectation, α-Fe_2O_3 and Fe_3O_4 are formed, and tribological properties in implanted samples are also enhanced.

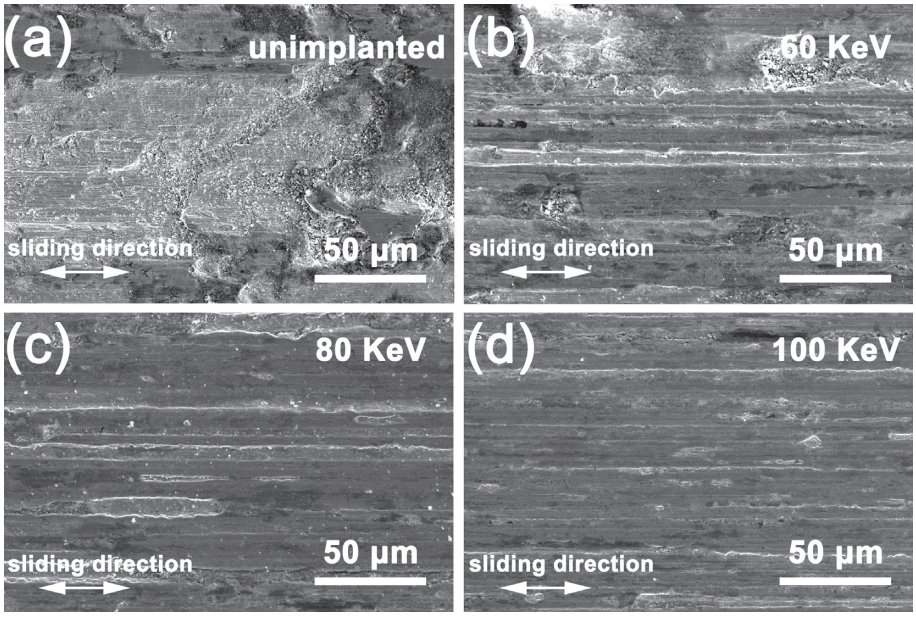

Figure 7: Micromorphologies of worn surfaces. (a) Unimplanted. (b) 60 keV. (c) 80 keV. (d) 100 keV.

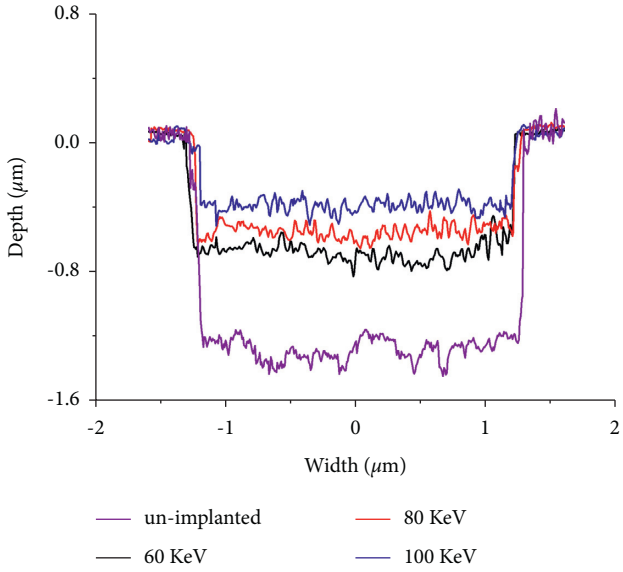

Figure 8: Depths of wear scar measured by surface profilometer. (a) Unimplanted. (b) 60 keV. (c) 80 keV. (d) 100 keV.

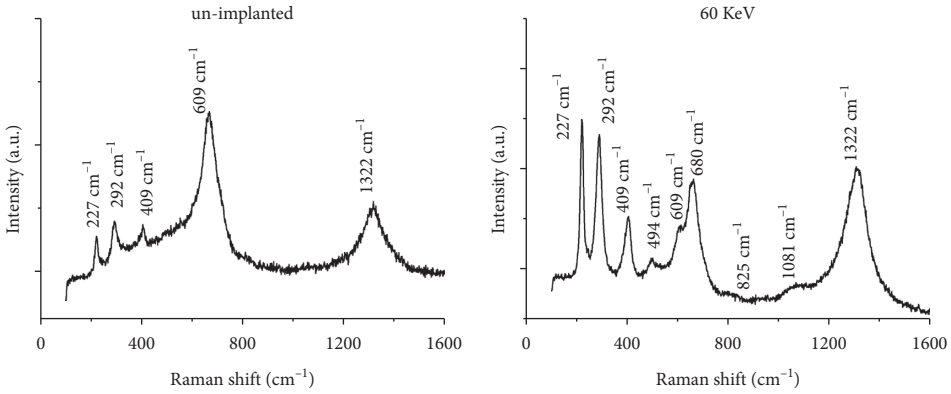

Figure 9: Continued.

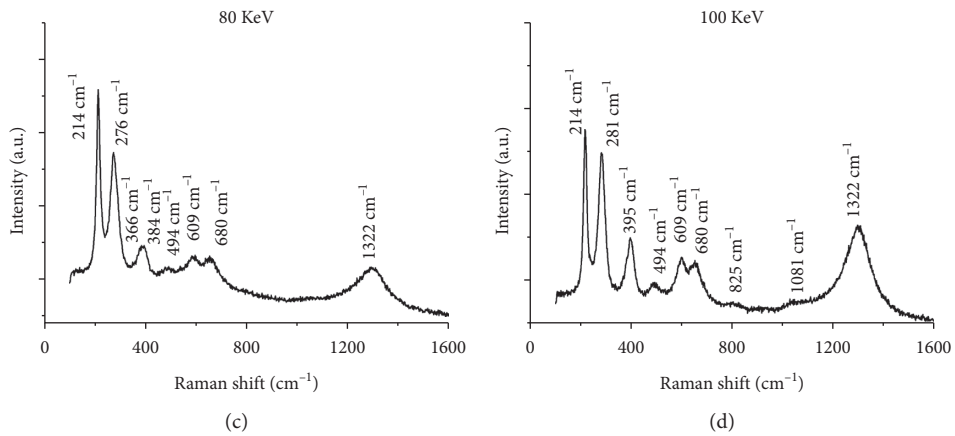

Figure 9: Raman spectroscopy of surface and wear scars. (a) Unimplanted. (b) 60 keV. (c) 80 keV. (d) 100 keV.

4. Conclusions

Nitrogen ion implantation improves AISI M50 steel tribological properties through modifications on the surface layers of the material. As the nitrogen ion-implanted energy increases, both implantation depth and microhardness increase. Material mechanical performance has been significantly improved, and microhardness of the implanted layer at energy 100 keV is 1.3 times greater than that in unimplanted samples. Nitrogen ion implantation at a higher implanted energy can more effectively and efficiently improve wear resistance, and wear life in samples at 100 keV before the steady stage is 4 times greater compared with that in samples at 60 keV. It has also been found that oxides α-Fe_2O_3 and Fe_3O_4 form the adhesive bonding between the interfaces of implanted samples and increase wear resistance. To sum up, the wear mechanism is still mainly adhesive wear upon nitrogen ion implantation, whereas adhesion resistance shows a trend of increase with nitrogen-implanted energy.

Data Availability

The research data used to support the findings of this study are included within the article.

Conflicts of Interest

The authors declare that there are no conflicts of interest regarding the publication of this paper.

Authors' Contributions

Xiangyu Xie and Chao Chen contributed equally to this work.

Acknowledgments

This research work was supported by the National Natural Science Foundation of China (Grant no. 51605105), the Major Science and Technology Project in Guizhou Province (Grant no. Q.K.H.Z.D.Z.X.Z[2019]3016), the Youth Science and Technology Talents Growth Fund of Education Department of Guizhou Province (Grant no. KY[2018]300), and special funding of Guiyang Science and Technology Bureau and Guiyang University (Grant no. GYU-KY-[2021]).

References

[1] H. K. D. H. Bhadeshia, "Steels for bearings," *Progress in Materials Science*, vol. 57, no. 2, pp. 268–435, 2012.

[2] G. S. Vasyliev and O. M. Kuzmenko, "Pitting suppression of aisi 316 stainless steel plates in conditions of ultrasonic vibration," *International Journal of Chemical Engineering*, vol. 2020, Article ID 6697227, 7 pages, 2020.

[3] P. Mukhopadhyay, P. S. Kannaki, M. Srinivas, and M. Roy, "Microstructural developments during abrasion of m50 bearing steel," *Wear*, vol. 315, no. 1-2, pp. 31–37, 2014.

[4] Q. Zhang, J. Luo, X. Y. Xie, J. Xu, and Z. H. Ye, "Experimental study on the skidding damage of a cylindrical roller bearing," *Materials*, vol. 13, no. 18, 2020.

[5] B. P. Abbott, R. Abbott, and T. D. Abbott, "Observation of gravitational waves from a binary black hole merger," *Physical Review Letters*, vol. 116, no. 6, 2016.

[6] J. Kusinski, S. Kac, A. Kopia et al., "Laser modification of the materials surface layer-a review paper," *Bulletin of the Polish Academy of Sciences, Technical Sciences*, vol. 60, no. 4, pp. 711–728, 2012.

[7] D. V. Nazarov, E. G. Zemtsova, A. Y. Solokhin, R. Z. Valiev, and V. M. Smirnov, "Modification of the surface topography and composition of ultrafine and coarse grained titanium by chemical etching," *Nanomaterials*, vol. 7, no. 1, 2017.

[8] I. Lampé, D. Beke, S. Biri et al., "Investigation of silver nanoparticles on titanium surface created by ion implantation technology," *International Journal of Nanomedicine*, vol. 14, pp. 4709–4721, 2019.

[9] S. Li, Y. Fan, H. Chen et al., "Manipulating the triboelectric surface charge density of polymers by low-energy helium ion irradiation/implantation," *Energy & Environmental Science*, vol. 13, no. 3, pp. 896–907, 2020.

[10] T. R. Rautray, R. Narayanan, and K.-H. Kim, "Ion implantation of titanium based biomaterials," *Progress in Materials Science*, vol. 56, no. 8, pp. 1137–1177, 2011.

[11] T. R. Rautray, R. Narayanan, T.-Y. Kwon, and K.-H. Kim, "Surface modification of titanium and titanium alloys by ion implantation," *Journal of Biomedical Materials Research Part B: Applied Biomaterials*, vol. 93B, no. 2, pp. 581–591, 2010.

[12] Z. Ba, Q. Dong, J. Yin et al., "Surface properties of mg-gd-zn-zr alloy modified by sn ion implantation," *Materials Letters*, vol. 190, pp. 90–94, 2017.

[13] P. Vlcak, J. Fojt, Z. Weiss, J. Kopeček, and V. Perina, "The effect of nitrogen saturation on the corrosion behaviour of ti-35nb-7zr-5ta beta titanium alloy nitrided by ion implantation," *Surface and Coatings Technology*, vol. 358, pp. 144–152, 2019.

[14] F. Wang, C. Zhou, L. Zheng, and H. Zhang, "Improvement of the corrosion and tribological properties of css-42l aerospace bearing steel using carbon ion implantation," *Applied Surface Science*, vol. 392, pp. 305–311, 2017.

[15] P. Budzynski, J. Filiks, P. Zukowski, K. Kiszczak, and M. Walczak, "Effect of mixed n and ar implantation on tribological properties of tool steel," *Vacuum*, vol. 78, no. 2-4, pp. 685–692, 2005.

[16] M. Szala, D. Chocyk, A. Skic, M. Kamiński, W. Macek, and M. Turek, "Effect of nitrogen ion implantation on the cavitation erosion resistance and cobalt-based solid solution phase transformations of hiped stellite 6," *Materials*, vol. 14, no. 9, 2021.

[17] S. Verma, P. Dubey, A. W. Selokar, D. K. Dwivedi, and R. Chandra, "Cavitation erosion behavior of nitrogen ion implanted 13cr4ni steel," *Transactions of the Indian Institute of Metals*, vol. 70, no. 4, pp. 957–965, 2017.

[18] M. Kaminski, P. Budzynski, M. Szala, and M. Turek, "Tribological properties of the stellite 6 cobalt alloy implanted with manganese ions," *IOP Conference Series: Materials Science and Engineering*, vol. 421, 2018.

[19] P. Budzynski, M. Kaminski, M. Turek, and M. Wiertel, "Impact of nitrogen and manganese ion implantation on the tribological properties of stellite 6 alloy," *Wear*, vol. 456, 2020.

[20] R. E. Stoller, M. B. Toloczko, G. S. Was, A. G. Certain, S. Dwaraknath, and F. A. Garner, "On the use of srim for computing radiation damage exposure," *Nuclear Instruments and Methods in Physics Research Section B: Beam Interactions with Materials and Atoms*, vol. 310, pp. 75–80, 2013.

[21] K. Suzuki, "Extended lindhard-scharf-schiott theory for ion implantation profiles expressed with pearson function," *Japanese Journal of Applied Physics*, vol. 48, no. 4, 2009.

[22] M. Y. Li, E. J. Knystautas, and M. Krishnadev, "Enhanced microhardness of four modern steels following nitrogen ion implantation," *Surface and Coatings Technology*, vol. 138, no. 2-3, pp. 220–228, 2001.

[23] J. Jin and T. Shao, "Effects of single- and dual-element ion implantation on tribomechanical properties of cronidur 30 bearing steel," *Surface and Coatings Technology*, vol. 344, pp. 303–311, 2018.

[24] K.-H. Zum Gahr, *Microstructure and Wear of Materials*, Elsevier, Amsterdam, Netherlands, 1987.

[25] A. Lassoued, B. Dkhil, A. Gadri, and S. Ammar, "Control of the shape and size of iron oxide (α-Fe2O3) nanoparticles synthesized through the chemical precipitation method," *Results in Physics*, vol. 7, pp. 3007–3015, 2017.

[26] Y. Ding, L. Zhang, Q. Liao, G. Zhang, S. Liu, and Y. Zhang, "Electromagnetic wave absorption in reduced graphene oxide functionalized with fe3o4/fe nanorings," *Nano Research*, vol. 9, no. 7, pp. 2018–2025, 2016.

[27] B. B. Nayak, O. P. N. Kar, D. Behera, and B. K. Mishra, "High temperature nitriding of grey cast iron substrates in arc plasma heated furnace," *Surface Engineering*, vol. 27, no. 2, pp. 99–107, 2011.

[28] S. Q. Wang, M. X. Wei, F. Wang, X. H. Cui, and C. Dong, "Transition of mild wear to severe wear in oxidative wear of h21 steel," *Tribology Letters*, vol. 32, no. 2, pp. 67–72, 2008.

Hindawi
International Journal of Chemical Engineering
Volume 2021, Article ID 7188649, 7 pages
https://doi.org/10.1155/2021/7188649

Research Article

Dispersion Performance of Polycarboxylate Terpolymers with Different Alkyl Side-Chain Lengths in Pesticide Suspension Concentrate

Xiaodong Yang,[1] Tianrui Ren ,[2] and Bo Zhang [2]

[1]*State Key Laboratory Breeding Base of Green Pesticide and Agricultural Bioengineering/Key Laboratory of Green Pesticide and Agricultural Bioengineering, Ministry of Education, Guizhou University, Guiyang 550025, China*
[2]*Shanghai Engineering Research Center of Green Energy Chemical Engineering, The Key Laboratory of Resource Chemistry of Ministry of Education, College of Chemistry and Materials Science, Shanghai Normal University, 100 Guilin Road, Shanghai 200234, China*

Correspondence should be addressed to Tianrui Ren; trren@shnu.edu.cn and Bo Zhang; zb830216@shnu.edu.cn

Received 23 May 2021; Accepted 9 August 2021; Published 18 August 2021

Academic Editor: Fernanda Casciatori

A versatile dispersant plays a critical role in the suspension stability of pesticide suspension concentrate (SC) systems. Herein, a series of novel acrylate ester-based polycarboxylate terpolymers (PTs) were designed as dispersant for pesticide suspension concentrate and successfully synthesized in aqueous solutions from the copolymerization of α-methacrylic acid, allyl polyoxyethylene ether, and acrylate (methyl acrylate, ethyl acrylate, and *n*-butyl acrylate). Terpolymers were characterized by FT-IR and ^{1}H-NMR to confirm their structure. The surface activities of PTs were evaluated according to critical micelle concentration (CMC) and the surface tension at CMC (γ_{CMC}). PT-3 with the longest alkyl side-chain length displayed the most superior surface activity due to its lowest CMC value compared with that of the other PTs. Additionally, the dispersion properties of PTs as dispersants in a 600 g/L imidacloprid SC were evaluated. Results showed that compared to the other two PTs, PT-3 contributes to the excellent dispersion properties on imidacloprid SC. Meanwhile, the obtained SC system exhibited shear thinning behavior under high-speed shearing showing typical features of pseudo-plastic non-Newtonian fluids, which conforms to the Herschel–Buckley model. Our results revealed that the effect of the alkyl side-chain length of dispersants could be considered the primary modulator of dispersion performance of SCs.

1. Introduction

Pesticide aqueous SC, as an eco-friendly water-based formulation, exhibits excellent advantages, such as high suspension and bioefficacy, low cost, and safety for operators [1, 2]. However, SC belongs to a thermodynamic and unstable dispersed system and easily encounters physical stability obstacles, such as Ostwald ripening and the flocculation or agglomeration of particles [3], which encloses lots of water and results in increasing the viscosity and decreasing the fluidity of SC. This is especially true for high-concentration SC. Ionic polymeric surfactants, which adsorbed onto solid particles and prevent the particles from aggregation because of electrostatic or steric repulsion, were often served as dispersants to address the above problems [4, 5]. Among these polymers, polyacrylic acid (PAA) is most widely used as a dispersant. Compared to PAA, the molecular structure of polycarboxylate copolymers is easy to be modified, which can meet specific properties for various applications.

Especially, polycarboxylate copolymers such as terpolymers are considered as a versatile dispersant because of their numerous branched chain groups, including carboxyl group, sulfonic acid group, amino group, and polyoxyethylene group side chains, which is widely used in concrete, ceramics, paints, and dye to obviously

improve suspension stability of the aqueous suspension system [6–9]. This is due to the fact that the carboxylate groups of the admixtures act as anchors to adsorb on the surface of the particles and show electrostatic effect. Meanwhile, the polyethylene oxide side chains also prevent the steric effect and prevent agglomeration of the particles [10–13]. For example, Wang et al. and Bai et al. found that the particular molecular structure of polycarboxylate-based terpolymers guaranteed their good dispersibility for $CaCO_3$ suspensions and had strong anti-redeposition power [14, 15]. Hence, it has great significance in designing suitable polycarboxylate terpolymers as dispersants for efficiently improving the stability of pesticide SC.

Imidacloprid is a chloro-nicotinyl insecticide which specifically blocks the microtinergic neuronal pathway, which is commonly used in rice, soyabean, maize, potatoes, vegetables, sugar beets, fruit, cotton, hops, and turf and is especially systemic when used as the seed or soil treatment [16]. Herein, three kinds of polycarboxylate terpolymers with different carbon side-chain lengths as an anchoring unit were designed and successfully synthesized. Moreover, the obtained PTs were selected as dispersants to prepare 600 g/L imidacloprid SC to verify its effect on the suspension stability of SC.

2. Experimental Section

2.1. Materials. Technical-grade imidacloprid (98.5% purity) was kindly supplied by Jiangsu Jiannong Agrochemical and Chemical Co. Ltd. (China). Allyl polyoxyethylene ether (APEG), α-methacrylic acid (MAA), methyl acrylate (MA), ethyl acrylate (EA), and n-butyl acrylate (BA) were obtained from Sinopharm Chemical Regent Co. (China). Xanthan gum was of food reagent grade and obtained from the Shanghai Ji Hu Chemical Co., Ltd of China. The SR-08 wetting agent was purchased from the Shanghai ShiDa Micromolecular Materials Co., Ltd. The ethylene glycol antifreeze agent was obtained from Shanghai Titan Technology Co., Ltd. Double distilled water was used in the experiment. All chemicals were of analytic grade and were used without further purification.

2.2. Synthesis of Polycarboxylate Terpolymers (PTs). Scheme 1 illustrates the synthesis of PTs by free-radical polymerization of APEG and MAA with MA, EA, and BA, which are denoted as PT-1, PT-2, and PT-3, respectively. The mole ratio of APEG: MAA: MA/EA/BA was 4 : 1 : 1. Specifically, 0.5 wt.% of initiator and 1 wt.% chain transfer agent were added to the monomers. Appropriate amounts of distilled water and sodium bisulfite (a certain amount of chain transfer agent, water, and methanol) were added into a 250 mL four-mouth flask and stirred at 80°C. APEG, MAA, and MA/EA/BA were dissolved in methanol and added dropwise into the reactor. Then, the mixture was allowed to react at 80°C for 3.5 h. Next, the mixture was cooled to room temperature and its pH was adjusted to 7-8 with 30 wt.% NaOH. Finally, the PTs were obtained.

2.3. Structural Characterization of PTs. The PTs were purified with a dialysis bag and the powder was obtained by freeze-drying. Infrared spectroscopy was analyzed by potassium bromide pellet method. Using deuterium instead of water as the solvent, the structure was characterized by ^{1}H NMR spectroscopy.

2.4. Measurement of Critical Micelle Concentration (CMC) Values of PTs. Surface tension of PT aqueous solutions was measured at 25°C with a JYW-2008 tensiometer (CDTM Ltd., China) by the Wilhelmy plate method. Prior to each experiment, the instrument was calibrated and checked by measuring the surface tension of distilled water. The CMC value was obtained from the breakpoint of the plot of surface tension (γ) versus ln c [17].

According to Gibbs law, the maximum surface excess concentration (Γ_{CMC}) and the minimum surface area per surfactant molecule (A_{CMC}) were calculated by the Gibbs adsorption isotherm equations (equations (1) and (2)). And, the Gibbs free energy of micellization, $\Delta G^{\theta}_{\mathrm{mic}}$, and the Gibbs free energy of adsorption $\Delta G^{\theta}_{\mathrm{ad}}$ were calculated using equations (3) and (4) [4].

$$\Gamma_{\mathrm{CMC}} = \frac{-1}{2.303nTR}\left(\frac{\partial\gamma}{\partial \lg C}\right)_T, \tag{1}$$

$$A_{\mathrm{cmc}} = \frac{1}{N_A\Gamma_{\mathrm{cmc}}}, \tag{2}$$

$$\Delta G^{\Theta}_{\mathrm{mic}} = nRT\ \ln \mathrm{CMC}, \tag{3}$$

$$\Delta G^{\Theta}_{\mathrm{ad}} = nRT\ \ln \mathrm{CMC} - 0.6023\left(\gamma_0 - \gamma_{\mathrm{cmc}}\right)A_{\mathrm{cmc}}, \tag{4}$$

where γ_0, N_A, and γ_{CMC} are the PTs of pure water, Avogadro's number, and the surfactant solutions at CMC, respectively. Here, n is the number of species at the interface whose concentration changes with surfactant concentration ($n = 1$ for a gemini surfactant and $n = 2$ for an anionic surfactant). R and T take their usual meanings.

2.5. Preparation of 600 g/L Imidacloprid SC. 600 g/L imidacloprid SCs were prepared by wet sand grinding technology. The optimum formulation of SCs was determined by pre-experiment. Typically, 50 g imidacloprid, 2 g PTs, 1 g wetting agent SR-08, 4 g xanthan gum, and 4 g ethylene glycol were mixed together with the rest of the water. Then, the mixture was obtained after grinding under room temperature until the particle size distribution of less than 3 μm.

2.6. Characterization of the 600 g/L Imidacloprid SC

2.6.1. Zeta Potential of 600 g/L Imidacloprid SC. A small amount of 600 g/L imidacloprid SC was weighed in a 250 mL beaker using an analytical balance. After diluting the imidacloprid to a given concentration by adding deionized water, the solution was transferred to a 50 mL centrifuge tube and centrifuged at 3000 r/min for 5 min. The zeta

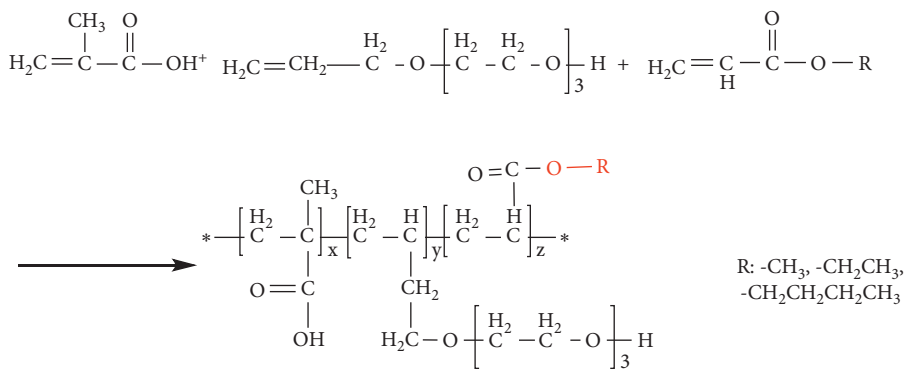

Scheme 1: Synthesis process of PTs.

potential of the supernatant of the centrifugation was measured on a Malvern Nano ZS90. Each sample was measured three times, and the average was used.

2.7. Measurement of Suspensibility of 600 g/L Imidacloprid SC

2.7.1. Suspensibility of 600 g/L Imidacloprid SC. The suspensibility of SC was measured according to GB/T 14825-2006.

2.7.2. Determination of SC Viscosity and Rheological Properties. The viscosity and rheological properties of the SC were measured using an Anton Par MCR 102 rotational rheometer. The shear viscosity of SC samples was studied at 25°C with a shear rate of 0–1000 s^{-1}.

Viscosity recovery as a critical factor of SC was measured in three stages. That is, the sample was subjected to a constant low-speed shear (0.25 s^{-1}) in the initial 25 s, high-speed shear (1000 s^{-1}) in the next 10 s, and then constant low-speed shear (0.25 s^{-1}) for recovery.

3. Results and Discussion

The chemical structures of PTs were analyzed by FT-IR and ^{1}H-NMR (Figure 1). Taking the case of PT-3, as presented in Figure 1(a), the wide stretching vibration peak of −OH is at 3394 cm^{-1}, the stretching vibration peaks of methyl and methylene appear at 2922 cm^{-1} and 2871 cm^{-1}, and the characteristic peak of C = O locates at 1735 cm^{-1}. A value of 1453 cm^{-1} is the bending vibration of methyl and methylene, 1109 cm^{-1} is the stretching vibration peak of C-O-C, and the characteristic peaks of double bond at 2500–2000 cm^{-1} disappear after copolymerization.

Figure 1(b) shows ^{1}H-NMR spectrum of PT-3. Among them, $\delta = 4.70$ is the solvent peak and $\delta = 3.8$–3.47 is the oxyethylene structural unit (CH_2CH_2O) in the polyether. The proton peak of H on the main carbon chain is at $\delta = 1.36$–1.58, and the proton peaks of $-CH_3$ and $-CH_2$ are near $\delta = 0.9$. After $\delta = 5.7$, there is no double bond proton peak, indicating that it disappears and participates in the reaction polymerization.

Furthermore, the GPC analysis was utilized to obtain the molecular weight of various PTs and their distributions. The M_n and M_w/M_n of PTs are listed in Table 1. The M_n and M_w/M_n of PT-1, PT-2, and PT-3 are 2160, 2310, and 2287, and 2.47, 2.83, and 2.28, respectively. The results indicate that the various dispersants are randomly copolymerized by free-radical copolymerization.

3.1. CMC and Thermodynamic Properties. CMC and surface tension at this concentration (γ_{CMC}) are important factors to measure the surface activity of surfactant aqueous solutions. Figure 2 and Table 2 show the surface tension of PTs, from which we realize that the aqueous solution exhibited a continuous decrease of surface tension and remained unchanged with the concentration increasing to CMCs. Compared with other PTs, the CMC and γ_{CMC} values of PT-3 are minimum, which indicated that PT-3 has the most superior surface activity. The hydrophobic monomer BA makes PT-3 more hydrophobic, resulting in its lower CMC and γ_{CMC} [18].

The adsorption data of PTs are listed in Table 2. PT-3 has a largest Γ_{max} and smallest A_{min}, conferring its superior surface activity. Meanwhile, the negative values of ΔG_{mic} show the micellization process, and it is a thermodynamic spontaneous process. The order of absolute value of ΔG_{mic} is PT-3 > PT-2 > PT-1, which suggests that PT-3 has the strongest driving force for micellization or adsorption at the air-liquid interface [19]. This could be attributed to the greatest hydrophobic performances of PT-3, leading to an easier formation of micelles [20].

3.2. Impacts of Dispersant Dosage on Zeta Potential and Viscosity of 600 g/L Imidacloprid SC. Zeta potential is one of the key parameters usually utilized to estimate suspension stability, which reflects the effective adsorption of dispersants on the surface of particles. Figure 3(a) shows the effects of PTs on the zeta potential of 600 g/L imidacloprid SC. It was found that the amount of PTs dramatically affected the zeta potential. The zeta potential decreases sharply with increasing PTs from 0 to 2 wt.%. Moreover, the continued increase of the dispersant beyond 2 wt.% up to 6 wt.% decreases a little zeta potential, suggesting that the dispersants gradually reached saturation adsorption on the surface of pesticide particles at the concentration of 6 wt.%. Surprisingly, the zeta potential decreases with further increase in PT

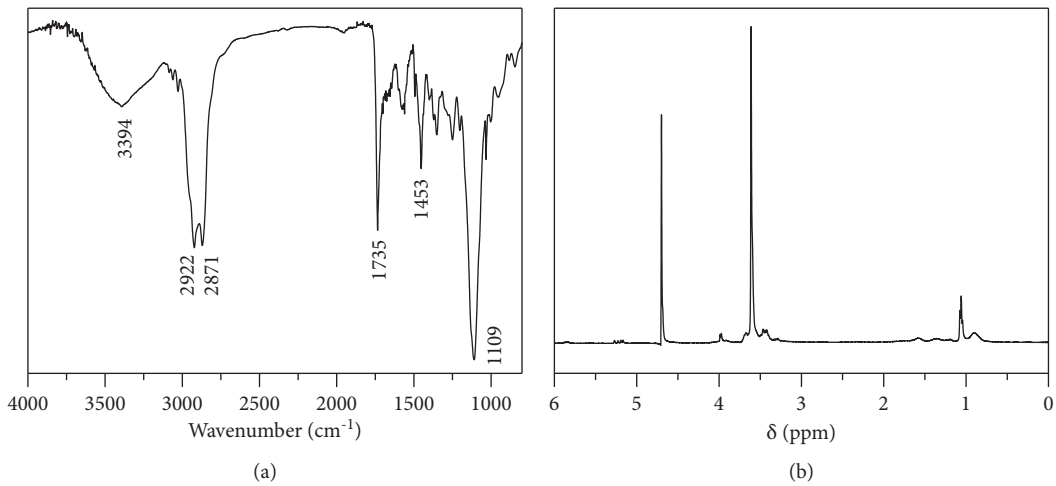

Figure 1: FTIR spectrum and ^{1}H-NMR spectra of PT-3.

Table 1: Monomer combination and GPC results for the various PTs.

Sample	Monomer Ratio					M_n (g/mol)	M_w/M_n
	MAA	APEG	MA	EA	BA		
PT-1	1	4	1			2160	2.47
PT-2	1	4		1		2310	2.83
PT-3	1	4			1	2287	2.28

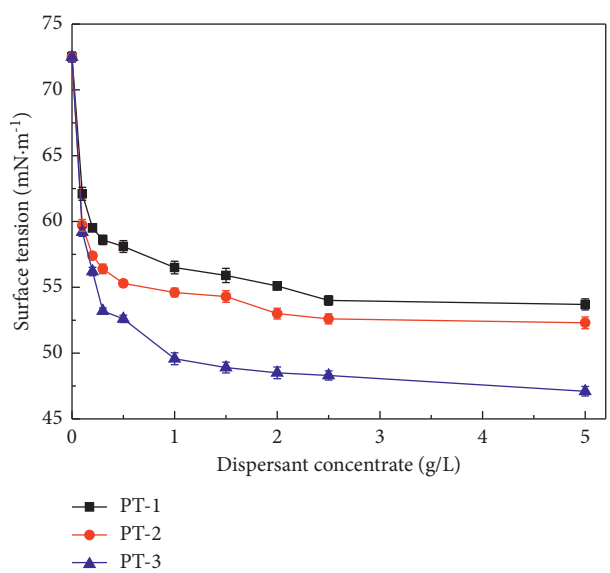

Figure 2: Evaluation of the CMC values of PTs by means of the Wilhelmy plate method.

Table 2: Surface properties of PTs.

Dispersants	γ_{CMC} (mN/m)	CMC (g/L)	Γ_{max} ($\times 10^{-6}$ mol/m^2)	A_{CMC} (nm^2/molecule)	ΔG_{mic} (kJ/mol)
PT-1	53.70	2.50	4.66	0.354	−20.728
PT-2	52.30	2.15	5.36	0.310	−22.854
PT-3	47.10	1.33	6.58	0.252	−24.498

dosage. This is because that excessive counterions of dispersants enter into the diffusion layer in the double electrical layer, resulting in the slight decrease in zeta potential values [21]. Additionally, the absolute of zeta potential of 600 g/L imidacloprid SC obtained from PT-3 is minimum, indicating that PT-3 could provide stronger electrostatic

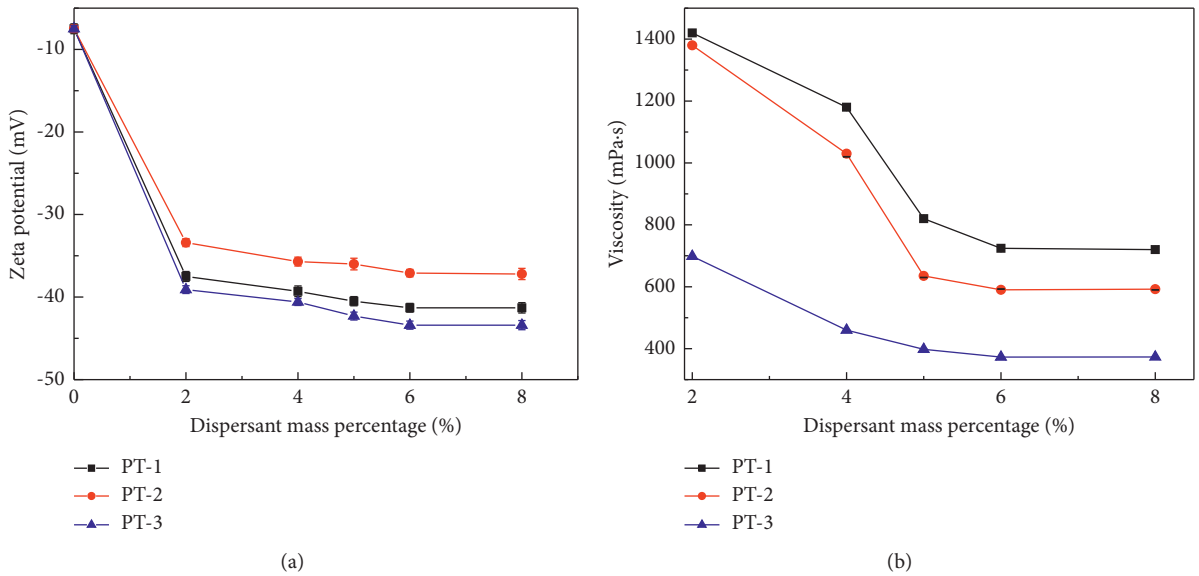

Figure 3: Impacts of PTs on zeta potential and viscosity of 600 g/L imidacloprid SC.

repulsion than PT-1 and PT-2. Hence, the optimal dispersant and additive amount are PT-3 and 6%, respectively.

The dispersant can effectively improve the viscosity of suspension systems and further effect on suspension stability. Subsequently, we investigated the effect of PT amounts on the viscosity of 600 g/L imidacloprid SC. As illustrated in Figure 3(b), it was found that the viscosity of imidacloprid SC sharply decreased and then slightly increased with increasing amounts of the PTs. When the dispersant dosage reached 6%, the viscosity of the SC is minimum, which agrees with the results of zeta potential (Figure 3(a)). However, when the amount of dispersants is above 6%, it leads to a slight increase in viscosity, which could be because that the excess dispersant causes counterions to enter the diffusion layer and the electrostatic repulsion decreases. Therefore, the combined bridging and depletion effects result in increased viscosity of the suspension system [19]. Notably, PT-3 reveals a greater influence on the viscosity of the SC, indicating that PT-3 exhibits superior dispersion capacity for SC.

We further investigated the thermal stability and rheological properties of 600 g/L imidacloprid SC made of PTs in 6 wt.% dosage.

3.3. Analysis of Thermal Stability of 600 g/L Imidacloprid SC. The physical stability of pesticide SC systems is of great significance for its long-term storage. The long-term storage stability is very important for pesticide formulations for practical usage in agriculture since delamination, caking, and degradation of the active pesticide may occur during storage. To study storage stability, the optimum SC samples made of PTs in 6 wt.% dosage were kept under $54 \pm 2^{\circ}$C for 14 days to determine their thermal stability (Table 3).

The changes of suspension rate and particle size distribution are important quality indexes and often used to characterize the physical stability of SC. As listed in Table 3, the suspension rate of the SC sample made of PT-3 is still greater than 95%, while the average diameter of particles is about 2.24 and 5.86 μm, respectively, before and after thermal storage, indicating PT-3 can effectively improve the physical stability of 600 g/L imidacloprid SC. Moreover, the SC prepared from PT-3 has suitable viscosity and viscosity change after thermal storage. Accordingly, the PT-3 is a promising dispersant for improving the thermal stability of 600 g/L imidacloprid SC.

3.4. Analysis of Rheological Properties of 600 g/L Imidacloprid SC. The suspension stability of SC systems was investigated by the rheological method. Apparent viscosity and thixotropy can obviously reflect the suspension stability of the SC system [22, 23]. Figure 4 shows the rheological curves of the PTs with 600 g/L imidacloprid SC in 6 wt.% dosage. The apparent viscosity of SC systems decreases with increasing shear rate, suggesting that the SC systems exhibited shear thinning behavior. Thus, three SCs had the characteristics of typical non-Newtonian pseudo-plastic fluid.

The three-stage thixotropy was used to verify the viscosity recovery of SC systems and can reflect the relationship between the viscosity and the change of network structure of the SC system. The results of the three-step thixotropy test are shown in the illustration of Figure 4(b). At low-speed shear, the spatial network structure of the SCs is stable and the systems exhibit high viscosity. Moreover, when the shear rate reached 1000 s^{-1}, the structures of SC systems were damaged, resulting in a rapid decline in viscosity. In the third stage (0.25 s^{-1} after 35 s), the structure of the SC system was restored. Notably, SC obtained from PT-3 had a higher structural recovery than SCs made of PT-1 and PT-2, indicating that SC made of PT-3 had higher stability, which is in accordance with the results of thermal stability (Table 3).

Table 3: The performances of 600 g/L imidacloprid SC before (*A*) and after (*B*) thermal storage.

Sample	Viscosity (MPa·s)		Suspension rate (%)		Particles size (μm)	
	A	*B*	*A*	*B*	*A*	*B*
PT-1	724	1265	92.8 ± 0.3	89.4 ± 0.1	2.13	8.33
PT-2	590	972	94.6 ± 0.5	90.2 ± 0.2	2.17	7.36
PT-3	373.4	525	96.3 ± 0.5	95.6 ± 0.3	2.24	5.86

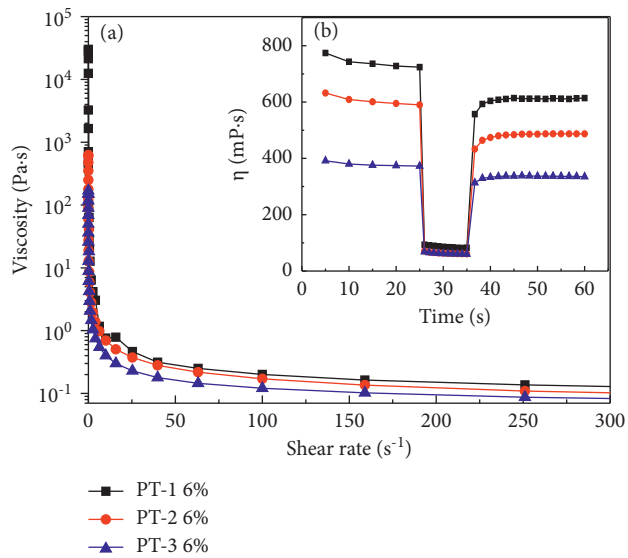

Figure 4: Rheological properties (a) and three-stage shearing curve (b) of 600 g/L imidacloprid SC.

3.5. The Proposed Stability Mechanism of Imidacloprid SC Prepared from PTs. When the pesticide particles were dispersed into aqueous solution, the particles were first wetted by water, and by increasing the wettability of the pesticide surface, dispersants reduce the frequently observed tendency of hydrophobic pesticide particles to spontaneously aggregate in aqueous suspensions; thus, the lower the surface tension of the dispersant aqueous solutions is, the easier the wetting of pesticide particles will be so as to contribute to the dispersion of pesticide particles more readily into aqueous solution [4, 24]. Compared with PT-1 and PT-2, PT-3 had the lowest CMC (Table 2). Therefore, PT-3 exhibits much better strong adsorption and wetting ability at the pesticide surface.

Remarkably, PT-3 has carboxylate groups and the longest hydrophobic alkyl side chain, as the anchoring points, which make it steadily be adsorbed on the surface imidacloprid particles. Meanwhile, PTs contain neutral EO pendants, which provide steric hindrance among imidacloprid particles. For the above reasons, PT-3 is endowed with a superior ability to stabilize and disperse imidacloprid particles and maintained the suspension stability of imidacloprid SC.

4. Conclusion

Three polycarboxylate terpolymers containing different carbon side-chain lengths were successfully synthesized by free-radical polymerization. PT-3 serves as an effective dispersant to stabilize the 600 g/L imidacloprid SC. When PT-3 dosage reached 6%, the SC had the minimum viscosity and the maximum zeta potential, which are very beneficial for improving its suspension stability. Meanwhile, rheological properties showed further evidence that the SC made of PT-3 exhibits excellent suspension stability compared to other PTs.

Data Availability

The data used to support the findings of this study are included within the article.

Conflicts of Interest

The authors declare that they have no conflicts of interest.

Acknowledgments

The authors thank the Chinese Characters of Shanghai Agricultural Sciences (2018) (No. 3-3).

References

[1] R. Peng, Y. Pang, X. Qiu, Y. Qian, and M. Zhou, "Synthesis of anti-photolysis lignin-based dispersant and its application in pesticide suspension concentrate," *RSC Advances*, vol. 10, no. 23, pp. 13830–13837, 2020.

[2] X. Qiu, W. Zeng, W. Yu et al., "Alkyl chain cross-linked sulfobutylated lignosulfonate: a highly efficient dispersant for carbendazim suspension concentrate," *ACS Sustainable Chemistry & Engineering*, vol. 3, no. 7, pp. 1551–1557, 2015.

[3] T. Tadros, P. Izquierdo, J. Esquena, and C. Solans, "Formation and stability of nano-emulsions," *Advances in Colloid and Interface Science*, vol. 108-109, pp. 303–318, 2004.

[4] L. Zhang, X. Guo, B. Zhang, and T. Ren, "Synthesis of nonylphenol polyoxyethylene oligomer and application as an effective dispersant in pyraclostrobin suspension concentrate," *Designed Monomers and Polymers*, vol. 22, no. 1, pp. 122–129, 2019.

[5] S. Haas, H.-W. Hässlin, and C. Schlatter, "Influence of polymeric surfactants on pesticidal suspension concentrates: dispersing ability, milling efficiency and stabilization power," *Colloids and Surfaces A: Physicochemical and Engineering Aspects*, vol. 183–185, pp. 785–793, 2001.

[6] K. Amini, A. Ghasemi, S. Soleimani Amiri, S. Mirvalad, and A. Habibnejad Korayem, "The synergic effects of metakaolin and polycarboxylate-ether on dispersion of graphene oxide in cementitious environments and macro-level properties of graphene oxide modified cement composites," *Construction and Building Materials*, vol. 270, Article ID 121462, 2021.

[7] Y. Li, Y. Zhang, J. Zheng et al., "Dispersion and rheological properties of concentrated kaolin suspensions with polycarboxylate copolymers bearing comb-like side chains," *Journal of the European Ceramic Society*, vol. 34, no. 1, pp. 137–146, 2014.

[8] F. Najafi, Z. Ranjbar, B. Shirkavand Hadavand, and S. Montazeri, "Synthesis and characterization of comb polycarboxylic acid dispersants for coatings," *Journal of Applied Polymer Science*, vol. 126, no. 3, pp. 877–881, 2012.

[9] H. Gharanjig, K. Gharanjig, and A. Khosravi, "Effects of the side chain density of polycarboxylate dispersants on dye dispersion properties," *Coloration Technology*, vol. 135, no. 2, pp. 160–168, 2019.

[10] X. Qiu, X. Peng, C. Yi, and Y. Deng, "Effect of side chains and sulfonic groups on the performance of polycarboxylate-type superplasticizers in concentrated cement suspensions," *Journal of Dispersion Science and Technology*, vol. 32, no. 2, pp. 203–212, 2011.

[11] J. Liu, Q. Ran, C. Miao, and M. Qiao, "Effects of grafting densities of comb-like copolymer on the dispersion properties of concentrated cement suspensions," *Materials Transactions*, vol. 53, no. 3, pp. 553–558, 2012.

[12] C.-Z. Li, N.-Q. Feng, Y.-D. Li, and R.-J. Chen, "Effects of polyethlene oxide chains on the performance of polycarboxylate-type water-reducers," *Cement and Concrete Research*, vol. 35, no. 5, pp. 867–873, 2005.

[13] B. Felekoglu and H. Sarıkahya, "Effect of chemical structure of polycarboxylate-based superplasticizers on workability retention of self-compacting concrete," *Construction and Building Materials*, vol. 22, no. 9, pp. 1972–1980, 2008.

[14] G. Wang, Y. Bai, X. Ma, W. Wang, Q. Yin, and Z. Du, "Effects of the PEG length of polycarboxylate-based terpolymers on their dispersion properties," *Journal of Molecular Liquids*, vol. 225, pp. 333–338, 2017.

[15] Y. Bai, X. Ma, W. Wang, Q. Yin, Z. Du, and G. Wang, "Synthesis, aggregation and dispersity properties of novels amphiphilic comb-like terpolymers," *Colloids and Surfaces A: Physicochemical and Engineering Aspects*, vol. 526, pp. 40–47, 2017.

[16] K. A. Sumon, A. K. Ritika, E. T. H. M. Peeters et al., "Effects of imidacloprid on the ecology of sub-tropical freshwater microcosms," *Environmental Pollution*, vol. 236, pp. 432–441, 2018.

[17] W. Zhang, G. J. Dong, H. Yang, J. Sun, J. Zhou, and J. Wang, "Synthesis, surface and aggregation properties of a series of amphiphilic dendritic copolymers," *Colloids and Surfaces A: Physicochemical and Engineering Aspects*, vol. 348, no. 1–3, pp. 45–48, 2009.

[18] R. Hoogenboom, D. Popescu, W. Steinhauer, H. Keul, and M. Möller, "Nitroxide-mediated copolymerization of 2-hydroxyethyl acrylate and 2-hydroxypropyl acrylate: copolymerization kinetics and thermoresponsive properties," *Macromolecular Rapid Communications*, vol. 30, no. 23, pp. 2042–2048, 2009.

[19] C. Ren, F. Wang, Z. Zhang, H. Nie, N. Li, and M. Cui, "Synthesis, surface activity and aggregation behavior of gemini imidazolium surfactants 1, 3-bis (3-alkylimidazolium-1-yl) propane bromide," *Colloids and Surfaces A: Physicochemical and Engineering Aspects*, vol. 467, pp. 1–8, 2015.

[20] P. Raffa, D. A. Z. Wever, F. Picchioni, and A. A. Broekhuis, "Polymeric surfactants: synthesis, properties, and links to applications," *Chemical Reviews*, vol. 115, no. 16, pp. 8504–8563, 2015.

[21] I. Grillo and J. Penfold, "Self-assembly of mixed anionic and nonionic surfactants in aqueous solution," *Langmuir*, vol. 27, no. 12, pp. 7453–7463, 2011.

[22] B. A. Moreira, F. de Oliveira Arouca, and J. J. R. Damasceno, "Analysis of suspension sedimentation in fluids with rheological shear-thinning properties and thixotropic effects," *Powder Technology*, vol. 308, pp. 290–297, 2017.

[23] M. A. Faers and G. R. Kneebone, "Application of rheological measurements for probing the sedimentation of suspension concentrate formulations," *Pesticide Science*, vol. 55, no. 3, pp. 312–325, 1999.

[24] D. Das, U. Dash, J. Meher, and P. K. Misra, "Improving stability of concentrated coal-water slurry using mixture of a natural and synthetic surfactants," *Fuel Processing Technology*, vol. 113, pp. 41–51, 2013.